Mon. Not. R. Astron. Soc. **000**, 1–?? (0000) Printed 20 July 2005 (MN LaTeX style file v2.2)

# Turbulent gas motions in galaxy cluster simulations: The role of SPH viscosity

K.Dolag[1],[2⋆], F. Vazza[1], G. Brunetti[3], G. Tormen[1]
[1] *Dipartimento di Astronomia, Universita di Padova, vicolo dell'Osservatorio 2, 35122 Padova, Italy*
[2] *Max-Planck-Institut für Astrophysik, Garching, Germany*
[3] *INAF, Istituto di Radioastronomia, via P.Gobetti 101, 40129 Bologna, Italy*

Accepted ???. Received ???; in original form ???

**ABSTRACT**
Smoothed particle hydrodynamics (SPH) employs an artificial viscosity to properly capture hydrodynamical shock waves. In its original formulation, the resulting numerical viscosity is large enough to suppress structure in the velocity field on scales well above the nominal resolution limit, and to damp the generation of turbulence by fluid instabilities. This could artificially suppress random gas motions in the intracluster medium (ICM), which are driven by infalling structures during the hierarchical structure formation process. We show that this is indeed the case by analysing results obtained with an SPH formulation where an individual, time-variable viscosity is used for each particle, following a suggestion by Morris & Monaghan (1997). Using test calculations involving strong shocks, we demonstrate that this scheme captures shocks as well as the original formulation of SPH, but, in regions away from shocks, the numerical viscosity is much smaller. In a set of nine high-resolution simulations of cosmological galaxy cluster formation, we find that this low–viscosity formulation of SPH produces substantially higher levels of turbulent gas motions in the ICM, reaching a kinetic energy content in random gas motions (measured within a 1Mpc cube) of up to 5%-30% of the thermal energy content, depending on cluster mass. This has also significant effects on radial gas profiles and bulk cluster properties. We find a central flattening of the entropy profile and a reduction of the central gas density in the low–viscosity scheme. As a consequence, the bolometric X-ray luminosity is decreased by about a factor of two. However, the cluster temperature profile remains essentially unchanged. Interestingly, this tends to reduce the differences seen in SPH and adaptive mesh refinement simulations of cluster formation. Finally, invoking a model for particle acceleration by MHD waves driven by turbulence, we find that efficient electron acceleration and thus diffuse radio emission can be powered in the clusters simulated with the low viscosity scheme provided that more than 5%-10% of the turbulent energy density is associated with Fast Magnetosonic Modes.

**Key words:** hydrodynamics, turbulence – methods: numerical – galaxies: clusters: general

## 1 INTRODUCTION

In hierarchical cold dark matter cosmologies, large structures form through the accretion of smaller structures (e.g., White et al. 1993). In particular, mergers and infall of halos play a fundamental role in determining the structure and dynamics of massive clusters of galaxies, where mergers can induce large–scale bulk motions with velocities of the order of $\sim 1000$ km s$^{-1}$ or larger. This results in complex hydrodynamic flows where most of the kinetic energy is quickly dissipated to heat by shocks, but some part may in principle also excite long-lasting turbulent gas motions.

Numerical simulations of merging clusters (e.g., Schindler & Mueller 1993; Roettiger et al. 1997; Ricker & Sarazin 2001; Takizawa 2005) provide a detailed description of the gas-dynamics during a merger event. It has been shown that infalling sub-clusters can generate laminar bulk flows through the primary cluster and inject turbulent eddies via Kelvin-Helmholtz (KH) instabilities at interfaces between the bulk flows and the primary cluster gas. Such eddies redistribute the energy of the merger through the cluster volume in a few turnover times, which corresponds to a time interval of order 1 Gyr. The largest eddies decay with time into more random and turbulent velocity fields, eventually developing a turbulent cascade with a spectrum of fluctuations expected to be close to a Kolmogorov spectrum.

Observationally, spatially resolved gas pressure maps of the Coma cluster obtained from a mosaic of XMM–Newton observation have indeed revealed the signature of mildly supersonic turbulence, at least in the central regions of the cluster (Schuecker et al.

⋆ E-mail: kdolag@mpa-garching.mpg.de

2004). It has also been suggested that the micro–calorimeters on-board of future X–ray satellites such as ASTRO-E2 should be able to detect the turbulent broadening of the lines of heavy ions in excess of the thermal broadening (Inogamov & Sunyaev 2003), which would represent a direct measurement of cluster turbulence.

Cluster turbulence could in principle store an appreciable fraction of the thermal energy of massive clusters, which would make it an important factor for understanding the structure of the ICM. Shear flows associated with cluster turbulence and the resulting dynamo processes could considerably amplify the magnetic field strength in the ICM (e.g., Dolag et al. 1999, 2002). In addition, magnetohydrodynamic waves can be efficiently injected in the ICM directly by shocks, by Kelvin-Helmholtz or Rayleigh-Taylor instabilities, or by the decay of turbulent eddies at larger scales. These waves, as well as shocks, can efficiently accelerate supra–thermal particles in the ICM to higher energies. Although there is still some debate concerning the detailed mechanism responsible for the origin of relativistic particles and magnetic fields in the ICM (e.g., Brunetti 2003), the presence of relativistic electrons and of $\sim \mu$G–strength magnetic fields in the ICM is proven by non–thermal emission studied with radio observations and possibly observations of hard X-Ray emission (e.g., Feretti et al. 2002; Fusco-Femiano et al. 2003,for a review). In addition, the occurrence of non–thermal phenomena is found to be related to the dynamical state and mass of the parent cluster (Giovannini et al. 1999; Buote 2001; Schuecker et al. 2001; Feretti 2002), which suggests a connection between cluster mergers and non–thermal activity.

Despite this potentially significant relevance of turbulence for the ICM, quantitative studies have received comparatively little attention in hydrodynamical cluster simulations thus far. One reason for this is that 3D turbulence is difficult to resolve in any numerical scheme, because these always introduce some finite numerical viscosity, effectively putting a limit on the Reynolds numbers that can still be adequately represented. In the Lagrangian SPH method, which has been widely employed for studies of cluster formation, an artificial viscosity is used to capture shocks. The original parameterisation of this viscosity (Monaghan & Gingold 1983) makes the scheme comparatively viscous; it smoothes out small-scale velocity fluctuations and viscously damps random gas motions well above the nominal resolution limit. This hampers the ability of the original SPH to develop fluid turbulence down to the smallest resolved scales.

However, the numerical viscosity of SPH can in principle be reduced by using a more sophisticated parameterisation of the artificial viscosity. Ideally, the viscosity should only be present in a hydrodynamical shock, but otherwise it should be negligibly small. To come closer to this goal, Morris & Monaghan (1997) proposed a numerical scheme where the artificial viscosity is treated as an independent dynamical variable for each particle, with a source term triggered by shocks, and an evolutionary term that lets the viscosity decay in regions away from shocks. In this way, one can hope that shocks can still be captured properly, while in the bulk of the volume of a simulation, the effective viscosity is lower than in original SPH. We adopt this scheme and implement it in a cosmological simulation code. We then apply it to high-resolution simulations of galaxy cluster formation, allowing us to examine a better representation of turbulent gas motions in SPH simulations of clusters. This also shines new light on differences in the results of cosmological simulations between different numerical techniques.

In Section 2, we discuss different ways of implementing the artificial viscosity in SPH. We demonstrate in Section 3 the robustness of our new low–viscosity scheme by applying it to several test problems. In Sections 4, 5 and 6, we introduce our set of cluster simulations, the algorithm to detect and measure turbulence, and the implications of the presence of turbulence for the structure and properties of galaxy clusters. In Section 7, we consider the effects of turbulence on the line-width of narrow X-ray metal lines. Finally, in Section 8 we apply the results from our new simulations to models for the production of radio emission due to turbulent acceleration processes. We give our conclusions in Section 9.

## 2 SIMULATION METHOD

The smoothed particle hydrodynamics method treats shocks with an artificial viscosity, which leads to a broadening of shocks and a relatively rapid vorticity decay. To overcome these problems, Morris & Monaghan (1997) proposed a new parameterisation of the artificial viscosity capable of reducing the viscosity in regions away from shocks, where it is not needed, while still being able to capture strong shocks reliably. We have implemented this method in the cosmological SPH code GADGET-2 (Springel 2005), and describe the relevant details in the following.

In GADGET-2, the viscous force is implemented as

$$\frac{\mathrm{d}v_i}{\mathrm{d}t} = -\sum_{j=1}^{N} m_j \Pi_{ij} \nabla_i \bar{W}_{ij}, \tag{1}$$

and the rate of entropy change due to viscosity is

$$\frac{\mathrm{d}A_i}{\mathrm{d}t} = -\frac{1}{2}\frac{\gamma-1}{\rho_i^{\gamma-1}} \sum_{j=1}^{N} m_j \Pi_{ij} v_{ij} \cdot \nabla_i \bar{W}_{ij}, \tag{2}$$

where $A_i = (\gamma-1)u_i/\rho_i^{\gamma-1}$ is the entropic function of a particle of density $\rho_i$ and thermal energy $u_i$ per unit mass, and $\bar{W}_{ij}$ denotes the arithmetic mean of the two kernels $W_{ij}(h_i)$ and $W_{ij}(h_j)$. The usual parameterisation of the artificial viscosity (Monaghan & Gingold 1983; Balsara 1995) for an interaction of two particles $i$ and $j$ includes terms to mimic a shear and bulk viscosity. For standard cosmological SPH simulations, it can be written as

$$\Pi_{ij} = \frac{-\alpha c_{ij} \mu_{ij} + \beta \mu_{ij}^2}{\rho_{ij}} f_{ij}, \tag{3}$$

for $\boldsymbol{r}_{ij} \cdot \boldsymbol{v}_{ij} \leqslant 0$ and $\Pi_{ij} = 0$ otherwise, i.e. the pair-wise viscosity is only non-zero if the particle are approaching each other. Here

$$\mu_{ij} = \frac{h_{ij} \boldsymbol{v}_{ij} \cdot \boldsymbol{r}_{ij}}{\boldsymbol{r}_{ij}^2 + \eta^2}, \tag{4}$$

$c_{ij}$ is the arithmetic mean of the two sound speeds, $\rho_{ij}$ is the average of the densities, $h_{ij}$ is the arithmetic mean of the smoothing lengths, and $\boldsymbol{r}_{ij} = \boldsymbol{r}_i - \boldsymbol{r}_j$ and $\boldsymbol{v}_{ij} = \boldsymbol{v}_i - \boldsymbol{v}_j$ are the inter-particle distance and relative velocity, respectively. We have also included a viscosity-limiter $f_{ij}$, which is often used to suppress the viscosity locally in regions of strong shear flows, as measured by

$$f_i = \frac{|\langle \boldsymbol{\nabla} \cdot \boldsymbol{v} \rangle_i|}{|\langle \boldsymbol{\nabla} \cdot \boldsymbol{v} \rangle_i| + |\langle \boldsymbol{\nabla} \times \boldsymbol{v} \rangle_i| + \sigma_i}, \tag{5}$$

which can help to avoid spurious angular momentum and vorticity transport in gas disks (Steinmetz 1996). Note however that the parameters describing the viscosity (with common choices $\alpha = 0.75 - 1.0$, $\beta = 2\alpha$, $\eta = 0.01 h_{ij}$, and $\sigma_i = 0.0001 c_i/h_i$ ) stay here fixed in time. This then defines the 'original' viscosity scheme usually employed in cosmological SPH simulations. We refer to runs performed with this viscosity scheme as *ovisc* simulations.

As a variant of the original parameterisation of the artificial viscosity, GADGET-2 can use a formulation proposed by Monaghan (1997) based on an analogy with Riemann solutions of compressible gas dynamics. In this case, $\mu_{ab}$ is defined as

$$\mu_{ij} = \frac{\boldsymbol{v}_{ij} \cdot \boldsymbol{r}_{ij}}{|\boldsymbol{r}_{ij}|}, \tag{6}$$

and one introduces a signal velocity $v_{ij}^{\rm sig}$, for example in the form

$$v_{ij}^{\rm sig} = c_i + c_j - 3\mu_{ij}. \tag{7}$$

The resulting viscosity term then changes into

$$\Pi_{ij} = \frac{-0.5\alpha v_{ij}^{sig}\mu_{ij}}{\rho_{ij}} f_{ij}. \tag{8}$$

We have also performed simulations using this signal velocity based artificial viscosity and found that it performs well in all test problems we examined so far, while in some cases it performed slightly better, in particular avoiding post shock oscillations in a more robust way. We refer to simulations performed using this 'signal velocity' based viscosity scheme as *svisc* simulations.

The idea proposed by Morris & Monaghan (1997) is to give every particle its own viscosity parameter $\alpha_i$, which is allowed to evolve with time according to

$$\frac{{\rm d}\alpha_i}{{\rm d}t} = -\frac{\alpha_i - \alpha_{\rm min}}{\tau} + S_i. \tag{9}$$

This causes $\alpha_i$ to decay to a minimum value $\alpha_{\rm min}$ with an e-folding time $\tau$, while the source term $S_i$ is meant to make $\alpha_i$ rapidly grow when a particle approaches a shock. For the decay timescale, Morris & Monaghan (1997) proposed to use

$$\tau = h_i \,/\, (c_i\, l), \tag{10}$$

where $h_i$ is the smoothing length, $c_i$ the sound speed and $l$ a free (dimensionless) parameter which determines on how many information crossing times the viscosity decays. For an ideal gas and a strong shock, this time scale can be related to a length scale $\delta = 0.447/l$ (in units of the smoothing length $h_i$) on which the viscosity parameter decays behind the shock front. For the source term $S_i$, we follow Morris & Monaghan (1997) and adopt

$$S_i = S^* f_i \, \max(0, -|\left<\boldsymbol{\nabla}\cdot\boldsymbol{v}\right>_i|), \tag{11}$$

where $\left<\boldsymbol{\nabla}\cdot\boldsymbol{v}\right>_i$ denotes the usual SPH estimate of the divergence around the particle $i$. Note that it would in principle be possible to use more sophisticated shock detection schemes here, but the simple criterion based on the convergence of the flow is already working well in most cases. We refer to simulations carried our with this 'low' viscosity scheme as *lvisc* runs.

Usually we set $S^* = 0.75$ and choose $l = 1$. We also restrict $\alpha_i$ to be in the range $\alpha_{\rm min} = 0.01$ and $\alpha_{\rm max} = 0.75$. Choosing $\alpha_{\rm min} > 0$ has the advantage, that possible noise which might be present in the velocity representation by the particles on scales below the smoothing length still will get damped with time. Increasing $S^*$ can give a faster response of the artificial viscosity to the shock switch without inducing higher viscosity than necessary elsewhere. We also note that we replace $\alpha$ in equation 3 (and equation 8 respectively) by the arithmetic mean $\alpha_{ij}$ of two interacting particles. Depending on the problem, we initialise $\alpha_i$ at the start of a simulation either with $\alpha_{\rm min}$ or $\alpha_{\rm max}$, depending on whether or not there are already shocks present in the initial conditions, respectively.

While the approach to reduce numerical viscosity with a time-variable $\alpha_i$ works well with both basic parameterisations of the artificial viscosity, most of our cosmological simulations were carried out with the 'original' parameterisation because the signal velocity variant became available in GADGET-2 only recently.

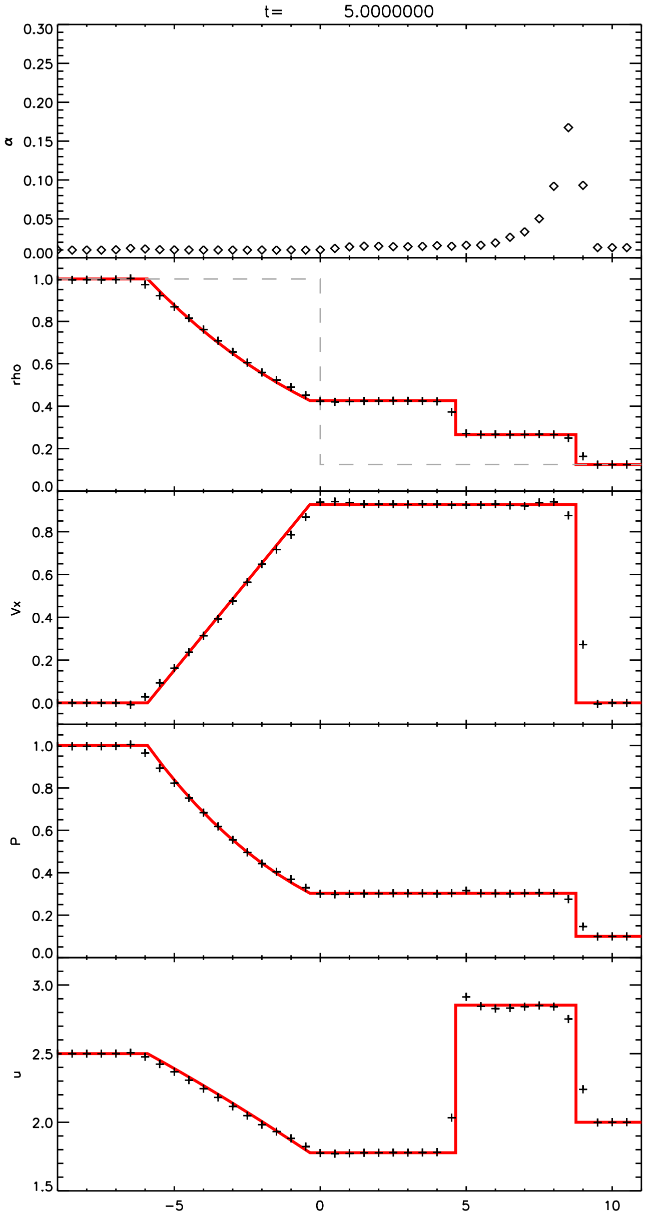


**Figure 1.** A standard shock tube problem (Sod 1978) computed with the low–viscosity scheme with an individual, time-dependent viscosity. From top to bottom, we show current value of the strength of the artificial viscosity $\alpha_i$, density, velocity, pressure, and internal energy, averaged for bins with spacing equal to the SPH smoothing length for particles in the low density region. The analytic solution of the problem for the time $t = 5.0$ is shown as a solid line.

## 3 TEST SIMULATIONS

To verify that the low–viscosity formulation of SPH with its time-dependent artificial viscosity is still able to correctly capture strong shocks, we computed a number of test problems. We here report on a standard shock tube test, and a spherical collapse test, which both have direct relevance for the cosmological formation of halos. As a more advanced test for the ability of the code to follow vorticity

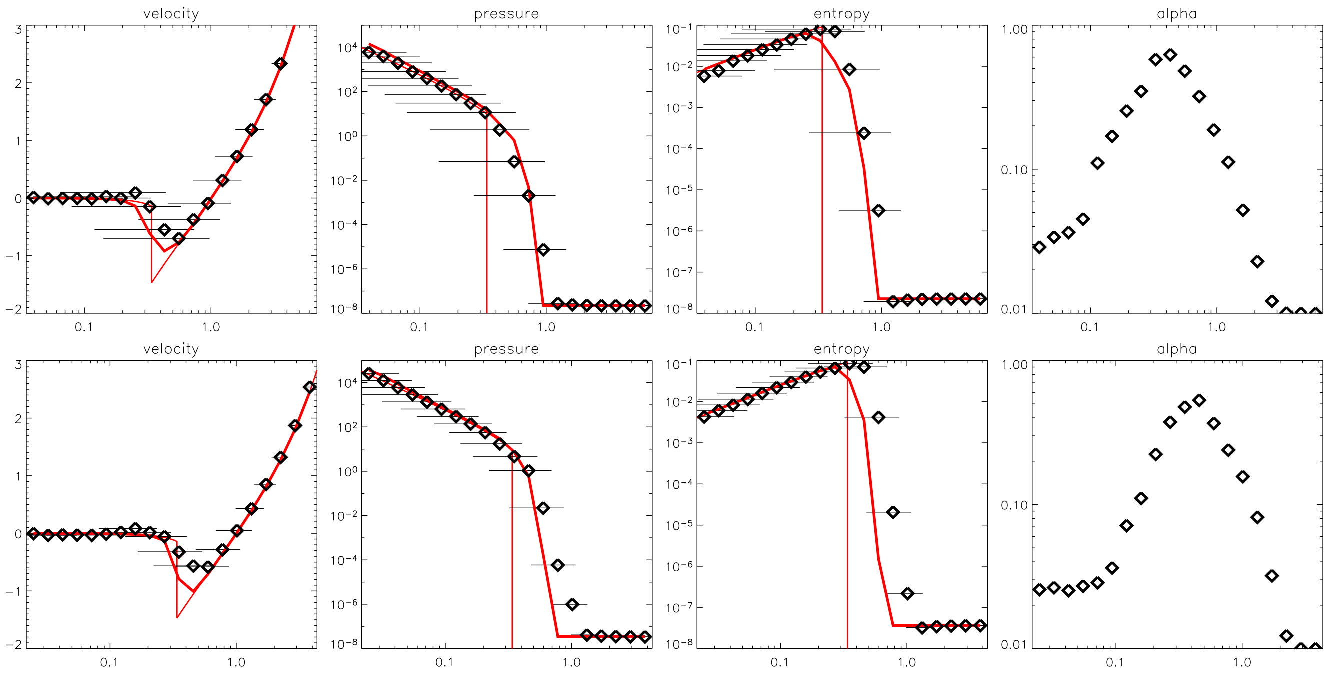


**Figure 2.** Profiles of velocity (left column), pressure (middle left column) entropy (middle right column) and viscosity constant $\alpha$ (right column) for the spherical collapse test at 2 different times (from top to bottom). The thin line marks the analytic solution, diamonds give the result obtained by the new SPH formulation for the time dependent viscosity. The thick line is the analytic solution adaptively smoothed with the SPH kernel, using the smoothing length of the particles in each bin. The lengths of the horizontal lines plotted at each data point correspond to the smoothing lengths of the SPH particles at this position.

generation, we investigate the problem of a strong shock striking an overdense cloud in a background medium. This test can also give hints whether turbulence is less strongly suppressed in the low–viscosity treatment of SPH than in the original formulation.

### 3.1 Shock-Tube Test

First, we computed a shock tube problem, which is a common test for hydrodynamical numerical schemes (Sod 1978). For definiteness, a tube is divided into two halves, having density $\rho_1 = 1$ and pressure $p_1 = 1$ on the left side, and $\rho_2 = 0.125$ and $p_2 = 0.1$ on the right side, respectively. Like in Sod (1978), we assume an ideal gas with $\gamma = 1.4$. To avoid oscillations in the post shock region (note that a shock is present in the initial conditions) we initialise the viscosity values of the particles with $\alpha_{\rm max} = 0.75$. We compute the test in 3D and make use of periodic boundary conditions. The initial particle grid is 5x5x50 on one half, and 10x10x100 on the other half, implying an equal particle mass for both sides.

In Figure 1, we show the state of the system at simulation time $t = 5$ in terms of density, velocity, and internal energy with a binning which corresponds to the smoothing length for particles in the low density region. We also include the analytic expectation for comparison. In addition, we plot the values of the artificial viscosity parameter of the particles. Clearly visible is that the viscosity is close to $\alpha_{\rm min}$ everywhere, except in the region close to the shock. One can also see how the viscosity builds up to its maximum value in the pre-shock region and decays in the post shock region. We note that the final post-shock state of the gas agrees well with the theoretical expectation, and is indistinguishable from the case where the original viscosity parameterisation is used.

### 3.2 Self-similar spherical collapse

A test arguably more relevant for cosmological structure formation is the self-similar, spherical collapse of a point perturbation in a homogeneous expanding background (Bertschinger 1985). This test is difficult for grid and SPH codes alike. The gas cloud collapses self similarly, forming a very strong shock (with formally has infinite Mach number) at the accretion surface. While grid codes with shock capturing schemes can usually recover the sharp shock surface very well, the large dynamic range in the post shock region with its singular density cusp, as well as the strict spherical symmetry of the problem, are challenging for mesh codes. On the other hand, Lagrangian SPH codes tend to have fewer problems with the central structure of the post-shock cloud, but they broaden the shock surface substantially, and typically show appreciable pre-shock entropy injection as result of the artificial viscosity.

We have computed the self-similar collapse test and compared the results for the new viscosity parameterisation with the analytic expectation. The very strong spherical shock of this problem is a particularly interesting test, because we can here test whether the low–viscosity formulation is still able to capture the strongest shocks possible.

In Figure 2, we show the structure of the shock at 2 consecutive times, scaled to the self-similar variables. In general, the SPH result recovers the analytic solution for the post-shock state very well, especially when the entropy profile is considered. However, the shock is substantially broadened, and some pre-heating in front of the shock is clearly visible. In the velocity field, some weak post-shock oscillations are noticable. We have also indicated the smoothing lengths of the SPH particles as horizontal error bars for each of the data points (the points at which the SPH kernel falls to zero is reached at twice this length). For comparison, we addition-

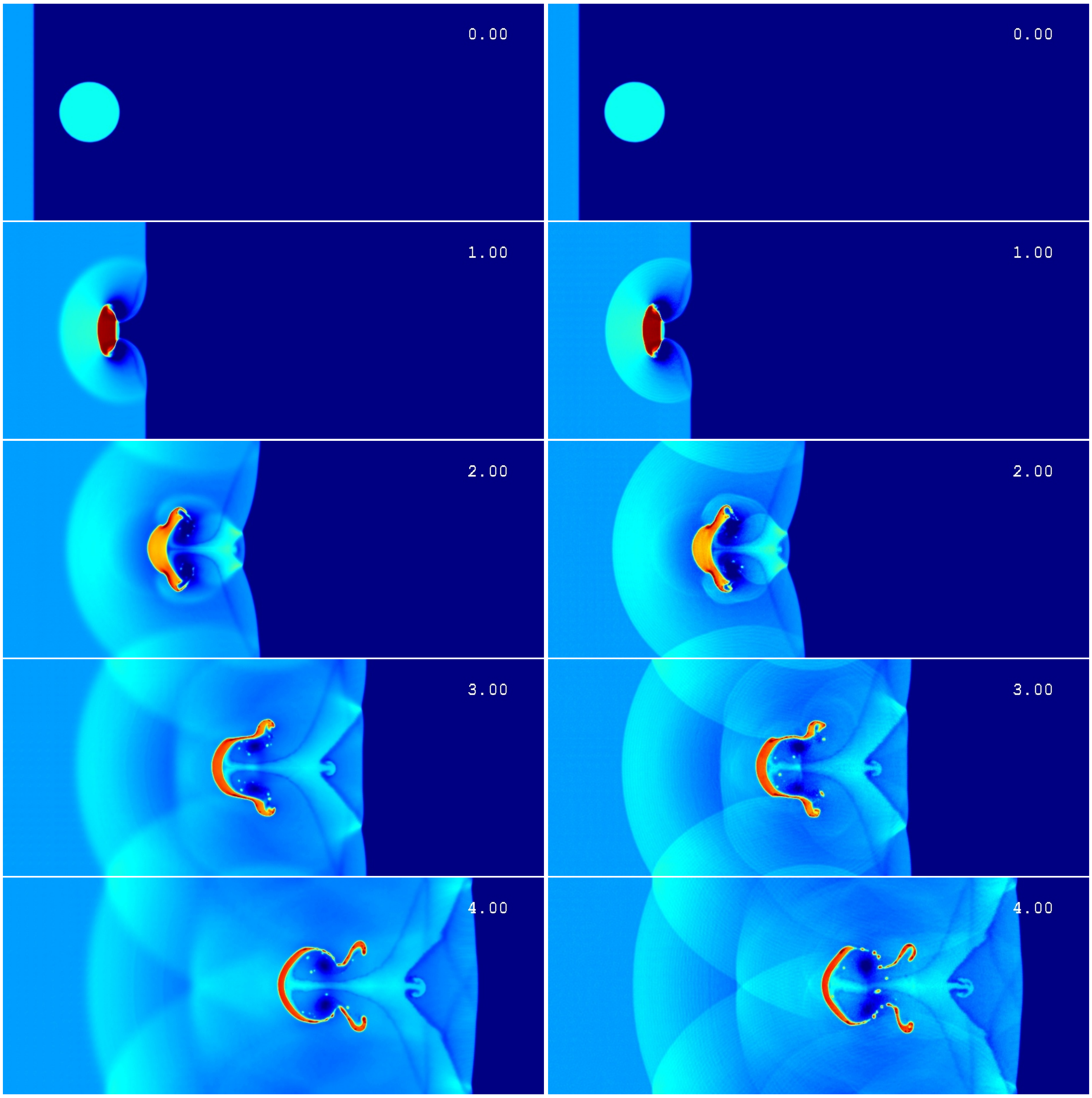


**Figure 3.** Time evolution of the interaction of a strong shock wave with an overdense cloud. We show the projected gas density and compare simulations carried out with original SPH (left) and the low–viscosity formulation (right). The incident shock wave has Mach number 10, and the cloud is initially at pressure equilibrium in the ambient medium and has overdensity 5.

ally over-plotted the analytic solution adaptively smoothed with the SPH kernel size at each bin.

The panels of the right column in Figure 2 show the profile of the viscosity parameter, which was set to $\alpha_{\rm min}$ at the beginning of the simulation, as the initial conditions do not contain a shock. The viscosity parameter builds up immediately after starting the simulation as the strong shock forms. Later one can see how the viscosity parameter begins to decay towards $\alpha_{\rm min}$ in the inner part, how it builds up to $\alpha_{\rm max}$ towards the shock surface, and how a characteristic profile develops as the shock moves outward. In the post-shock region an intermediate viscosity values is maintained for some time due to some non-radial motions of gas particles in this region.

### 3.3 Schock-cloud interaction

To verify that the low–viscosity scheme also works in more complex hydrodynamical situations, we simulate a test problem where a strong shock strikes a gas cloud embedded at pressure equilibrium in a lower density environment. A recent discussion of this setup can be found in Poludnenko et al. (2002) and references therein. SPH is able to reproduce the main features expected in this test non radiative

**Table 1.** Main characteristics of the non radiative galaxy cluster simulations. Column 1: identification label. Columns 2 and 3: mass of the dark matter ($M_{\rm DM}$) and gas ($M_{\rm gas}$) components inside the virial radius. Column 4: virial radius $R_{\rm v}$. Column 5: X-ray luminosity inside the virial radius $L_x$. Columns 6 and 7: mass-weighted temperature ($T_{\rm MW}$) and spectroscopic like temperature ($T_{\rm SL}$).

| Simulations | $M_{\rm DM}(h^{-1}10^{14}M_{\odot})$ | | $M_{\rm GAS}(h^{-1}10^{13}M_{\odot})$ | | $R_{\rm v}(h^{-1}$ kpc) | | $L_x(10^{44}\,{\rm erg\,s^{-1}})$ | | $T_{\rm MW}$(keV) | | $T_{\rm SL}$(keV) | |
|---|---|---|---|---|---|---|---|---|---|---|---|---|
| | svisc | lvisc | svisc | lvisc | svisc | lvisc | svisc | lvisc | svisc | lvisc | svisc | lvisc |
| g1 | 14.5 | 14.5 | 17.5 | 17.0 | 2360 | 2355 | 47.1 | 21.3 | 7.2 | 7.1 | 5.8 | 5.6 |
| g8 | 22.6 | 22.4 | 19.8 | 19.8 | 2712 | 2705 | 63.1 | 32.1 | 9.3 | 9.1 | 6.2 | 5.7 |
| g51 | 13.0 | 13.0 | 11.5 | 11.5 | 2255 | 2251 | 30.8 | 17.9 | 6.4 | 6.3 | 4.6 | 4.7 |
| g72 | 13.5 | 13.4 | 12.0 | 11.9 | 2286 | 2280 | 18.3 | 14.1 | 5.8 | 5.8 | 4.0 | 4.0 |
| g676 | 1.1 | 1.0 | 0.95 | 0.91 | 983 | 972 | 3.2 | 1.4 | 1.3 | 1.3 | 1.6 | 1.5 |
| g914 | 1.2 | 1.0 | 1.07 | 0.91 | 1023 | 971 | 4.2 | 1.7 | 1.4 | 1.3 | 1.6 | 1.7 |
| g1542 | 1.1 | 1.0 | 0.95 | 0.90 | 982 | 967 | 3.0 | 1.4 | 1.3 | 1.2 | 1.4 | 1.5 |
| g3344 | 1.1 | 1.1 | 1.00 | 0.96 | 1002 | 993 | 2.2 | 1.4 | 1.4 | 1.3 | 1.4 | 1.5 |
| g6212 | 1.1 | 1.1 | 1.00 | 1.01 | 1000 | 1006 | 3.0 | 1.5 | 1.3 | 1.3 | 1.6 | 1.7 |

problem reasonably well, like reverse and reflected shocks, back-flow, primary and secondary Mach stems, primary and secondary vortices, etc. (see Springel 2005). Our purpose here is to check whether the new scheme for a time-variable viscosity performs at least equally well as the original approach.

In Figure 3, we compare the time evolution of the projected gas density for the original viscosity scheme (left hand side) with the new low–viscosity scheme (right hand side). Overall, we find that the new scheme produces quite similar results as the original method. But there are also a number of details where the low–viscosity scheme appears to work better. One is the external reverse bow shock which is resolved more sharply with the new scheme compared to the original one. This is consistent with our findings from the previous tests, where we could also notice that shocks tend to be resolved somewhat sharper using the new scheme. We also note that instabilities along shear flows (e.g. the forming vortexes or the back-flow) are appearing at an earlier time, as expected if the viscosity of the numerical scheme is lower. This should help to resolve turbulence better.

In summary, the low–viscosity scheme appears to work without problems even in complex situations involving multiple shocks and vorticity generation, while it is still able to keep the advantage of a reduced viscosity in regions away from shocks. We can therefore expect this scheme to also work well in a proper environment of cosmological structure formation, and simulations should be able to benefit from the reduced viscosity characteristics of the scheme.

## 4 COSMOLOGICAL CLUSTER SIMULATIONS

We have performed high-resolution hydrodynamical simulations of the formation of 9 galaxy clusters. The clusters span a mass-range from $10^{14}\,h^{-1}{\rm M}_{\odot}$ to $2.3\times10^{15}h^{-1}{\rm M}_{\odot}$ and have originally been selected from a DM–only simulation (Yoshida et al. 2001) with box-size $479\,h^{-1}$Mpc of a flat $\Lambda$CDM model with $\Omega_0 = 0.3$, $h = 0.7$, $\sigma_8 = 0.9$ and $\Omega_{\rm b} = 0.04$. Using the 'Zoomed Initial Conditions' (ZIC) technique (Tormen et al. 1997), we then re-simulated the clusters with higher mass and force resolution by populating their Lagrangian regions in the initial conditions with more particles, adding additional small-scale power appropriately. The selection of the initial region was carried out with an iterative process, involving several low resolution DM-only resimulations to optimise the simulated volume. The iterative cleaning process ensured that all of our clusters are free from contaminating boundary effects out to at least 3 - 5 virial radii. Gas was introduced in the high–resolution region by splitting each parent particle into a gas and a DM particle. The final mass–resolution of these simulations was $m_{\rm DM} = 1.13\times10^9\,h^{-1}{\rm M}_{\odot}$ and $m_{\rm gas} = 1.7\times10^8\,h^{-1}{\rm M}_{\odot}$ for dark matter and gas within the high–resolution region, respectively. The clusters were hence resolved with between $2\times10^5$ and $4\times10^6$ particles, depending on their final mass. For details on their properties see Table 1. The gravitational softening length was $\epsilon = 5.0\,h^{-1}$kpc (Plummer–equivalent), kept fixed in physical units at low redshift and switched to constant comoving softening of $\epsilon = 30.0\,h^{-1}$kpc at $z \geqslant 5$. Additionally we re-simulated one of the smaller cluster (*g676*) with 6 times more particles (HR), decreasing the softening by a factor of two to $\epsilon = 2.5\,h^{-1}$kpc.

We computed three sets of simulations using non radiative gas dynamics, where each cluster was simulated three times with different prescriptions for the artificial viscosity. In our first set, we used the original formulation of artificial viscosity within SPH. In the second set, we used the parametrisation based on signal velocity, but with a fixed coefficient for the viscosity. Finally, in our third set, we employed the time dependent viscosity scheme, which we expect to lead to lower residual numerical viscosity. Our simulations were all carried out with an extended version of GADGET-2 (Springel 2005), a new version of the parallel TreeSPH simulation code GADGET (Springel et al. 2001). We note that the formulation of SPH used in this code follows the 'entropy-conserving' method proposed by Springel & Hernquist (2002).

## 5 IDENTIFYING TURBULENCE

In the idealized case of homegeneus and isotropic turbulence, the autocorrelation function of the velocity field of the fluid should not depend on the position (homogeneity) and it should only depend on the magnitude of the distance $\boldsymbol{r}$ between points (isotropy). The tensor of the correlation function of the velocities is thus given by (e.g. Choudhuri 1998):

$$R_{ij}(r) = \langle v_i(\boldsymbol{x}) v_j(\boldsymbol{x}+\boldsymbol{r})\rangle \qquad (12)$$

where $\boldsymbol{x}$ is the position of a fluid particle. The 3D power spectral density of the turbulent field is given by (e.g. Choudhuri 1998):

$$\Phi_{ij}(\boldsymbol{k}) = \frac{1}{(2\pi)^3}\int R_{ij}(\boldsymbol{r})\exp(i\,\boldsymbol{kr})\,{\rm d}\boldsymbol{r}. \qquad (13)$$

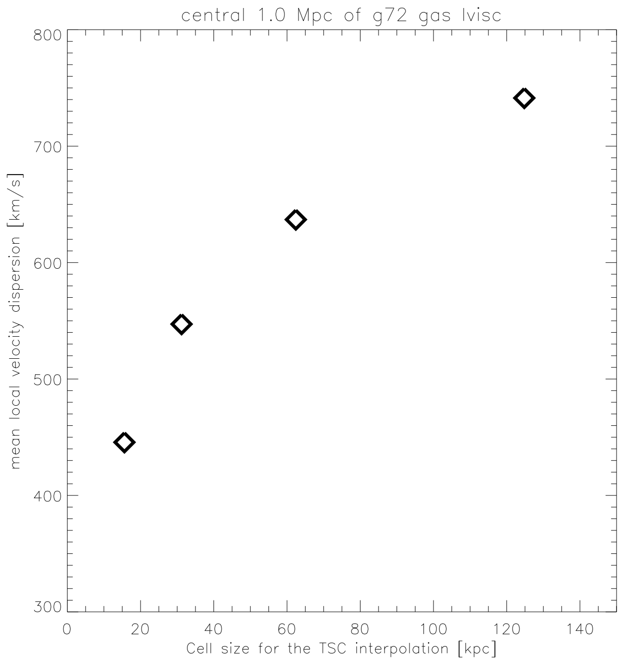


**Figure 4.** Mean local velocity dispersion for the central $500^3\mathrm{kpc}^3$ box as a function of the resolution adopted for the TSC–smoothing of the local mean field. Results are plotted for a low viscosity simulation.

The energy spectrum, $E(k)$, associated with the fluctuations of the velocity field is related to the diagonal parts of both the tensor of the correlation function, and that of the power spectral density. This energy spectrum is given by (e.g. Choudhuri 1998):

$$E(k) = 2\pi k^2 \Phi_{ii}(k), \tag{14}$$

and the total turbulent energy per unit mass is

$$u_{\rm turb} = \frac{1}{2}\left\langle v^2 \right\rangle = \frac{1}{2} R_{ii}(\boldsymbol{r}=0) = \int_0^\infty E(k)\,\mathrm{d}k, \tag{15}$$

where the summation convention over equal indices is adopted.

The real case of the intracluster medium is however much more complex, in particular not homogeneous and isotropic. The gravitational field induces density and temperature gradients in the ICM, and the continuous infall of substructures drives bulk motions through the ICM. These effects break both homogeneity and isotropy at some level, at least on the scale of the cluster, and thus demand a more complicated formalism to appropriately characterise the turbulent field. It is not the aim of the present paper to solve this problem completely. Instead we focus on a zero–order description of the energy stored in turbulence in the simulated boxes, and for this purpose the basic formalism described below should be sufficient.

A crucial issue in describing turbulent fields in the ICM is the distinction between large-scale coherent velocity field and small-scale 'random' motions. Unfortunately, the definition of a suitable mean velocity field is not unambiguous because the involved scale of averaging introduces a certain degree of arbitrariness. Perhaps the simplest possible procedure is to take the mean velocity computed for the cluster volume (calculated, for example, within a sphere of radius $R_{\rm vir}$) as the coherent velocity field, and then to define the turbulent velocity component as a residual to this velocity. This simple approach (hereafter *standard* approach) has been widely employed in previous works (e.g., Norman & Bryan 1999; Sunyaev et al. 2003), and led to the identification of ICM turbulence in these studies. However, an obvious problem with this method is that this global subtraction fail to distinguish a pure laminar bulk flow from a turbulent pattern of motion. Note that such a large scale laminar flows are quite common in cosmological simulations, where the growth of clusters causes frequent infalls and accretions of sub–halos. This infall of substructures is presumably one of the primary injection mechanisms of ICM turbulence.

To avoid this problem, a mean velocity field smoothed on scales smaller than the whole box can be used, and then the field of velocity fluctuations is defined by subtracting this mean–local velocity, $\overline{\boldsymbol{v}}(\boldsymbol{x})$, from the individual velocities $\boldsymbol{v}_i$ of each gas particle. We note that if the smoothing scale is chosen too small, one may risk loosing large eddies in the system if they are present, but at least this procedure does not overestimate the level of turbulence.

Following this second approach (hereafter *local–velocity* approach), we construct a mean local velocity field $\overline{\boldsymbol{v}}(x)$ on a uniform mesh by assigning the individual particles to a mesh with a *Triangular Shape Cloud* (TSC) window function. The mesh covers a region of 1.0 comoving Mpc on a side and typically has between $8^3$ and $64^3$ cells, which is coarse enough to avoid undersampling effects. The equivalent width of the TSC kernel is approximatively 3 grid cells in each dimension, corresponding to a smoothing scale of $\approx 360 - 45$ kpc, respectively. As our analysis is restricted only to the highest density region in the clusters, the scale for the TSC–smoothing is always larger than the SPH smoothing lengths for the gas particles, which typically span the range $7.5 - 15\,h^{-1}$kpc in the box we consider.

We then evaluate the local velocity dispersion at the position $\boldsymbol{x}$ of each mesh cell over all particles $a$ in the cell by:

$$\sigma_{ij}^2(\boldsymbol{x}) \simeq \langle [v_{a,i} - \bar{v}_i(\boldsymbol{x})]\,[v_{a,j} - \bar{v}_j(\boldsymbol{x})] \rangle_{\rm cell}\,, \tag{16}$$

where $i$ and $j$ are the indices for the three spatial coordinates, and $\langle\rangle_{\rm cell}$ denotes the average over particles within each cell.
The diagonal part of the tensor of the correlation function of the field of velocity fluctuations at $r=0$ in the simulated box can then be approximated by

$$R_{ii}(r=0) \simeq \left\langle \sigma_{ii}^2(\boldsymbol{x}) \right\rangle_{\rm Box}. \tag{17}$$

Based on Equation (15), we can then estimate the energy density of the turbulence in real space as

$$\rho(\boldsymbol{x}) \int E(k)\,\mathrm{d}k \sim \frac{1}{2}\rho(\boldsymbol{x}) \times \begin{cases} \left\langle \sigma_{ii}^2(\boldsymbol{x}) \right\rangle_{\rm box}\,, \\ \left\langle v_i^2(\boldsymbol{x}) \right\rangle_{\rm box}\,, \end{cases} \tag{18}$$

in the local–velocity and standard case, respectively. Here $\rho(\boldsymbol{x})$ is the gas density within the cells.

The subtraction of a local velocity from the velocity distribution of the particles is expected to efficiently filter out the contribution from laminar bulk–flows with a scale $\geqslant 3$ times the size of the cells used in the TSC smoothing. However, a large-scale turbulent velocity field component, if it exists, would also be suppressed, so that this procedure can be expected to reduce the turbulent velocity field to a certain degree. As shown in Figure 4, this depends on the resolution of the mesh used in the TSC assignment. Fig. 4 shows that the increase of the turbulent velocity dispersion with the cell size is not dramatic for cell sizes larger than 100 kpc. We find that (Vazza et al., in prep.) a TSC smoothing with larger cell sizes would not efficiently filter out contributions from laminar bulk–motions. It can be tentatively concluded that the local velocity approach with a smoothing with $16^3 - 32^3$ cells in the central $(1.0\,\mathrm{Mpc})^3$ volume catches the bulk of the turbulent velocity field in the simulated

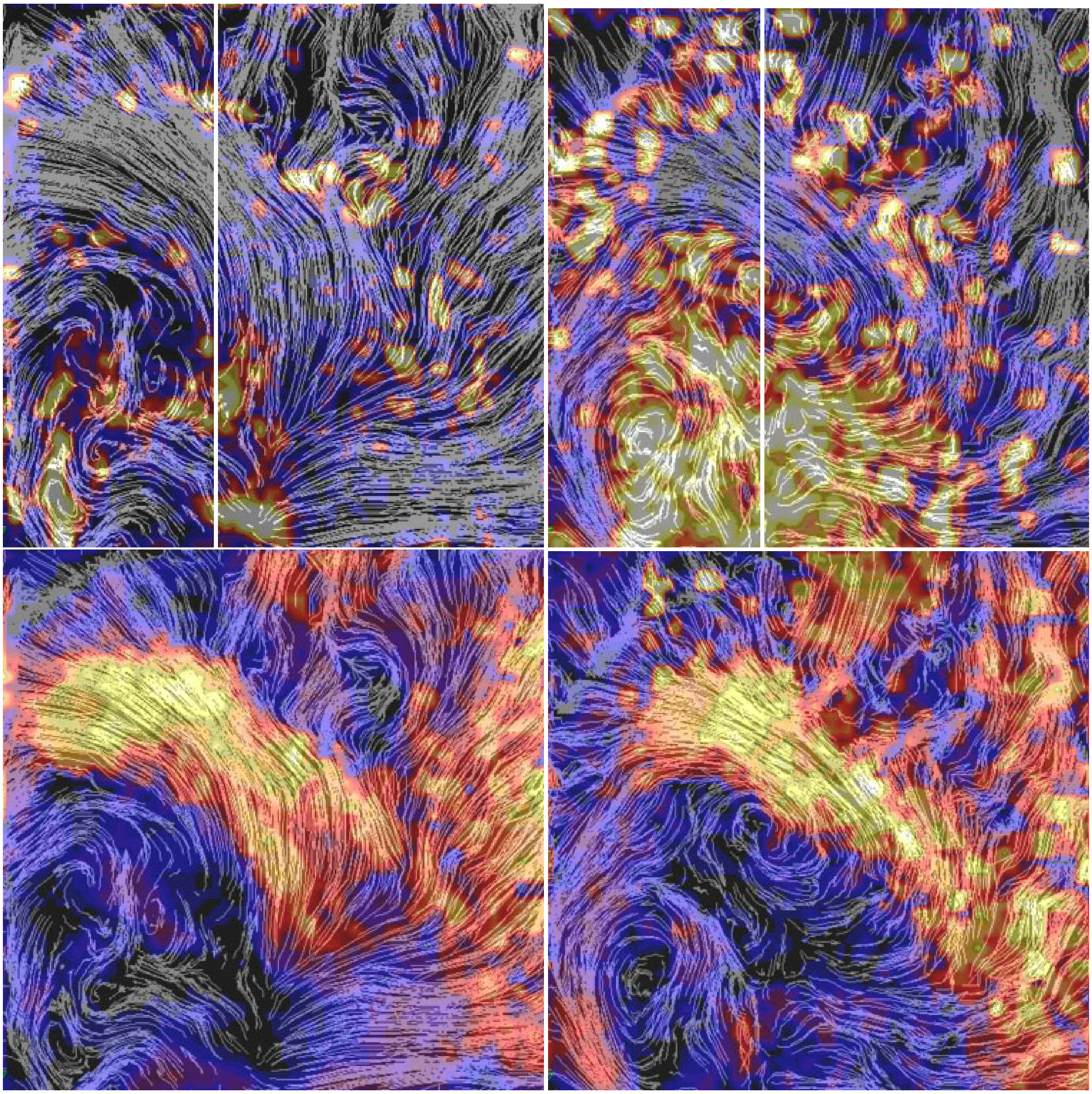

**Figure 5.** Gas velocity field in a slice through the central Mpc of a cluster simulation *g72* after subtracting the *global* mean bulk velocity of the cluster. The panels on the left is for a run with the original viscosity of SPH while the panels on the right shows the result for the low viscosity scheme. The underlying colour maps represent the turbulent kinetic energy content of particles, inferred using the local velocity method (upper row) or the standard velocity method (lower row). For the local velocity method a conservative $64^3$ grid is used in the TSC smoothing. The cluster centre is just below the lower-left corner of the images. The vertical lines in the upper row show where the 1–dimensional profile for the simulated radio–emission of Fig. 19 are taken.

box. Therefore, if not specified otherwise, all the numerical quantities given in the following are obtained using a TSC–assignment procedure based on $32^3$ cells. A more detailed discussion of this method and tests of the parameters involved is reported elsewhere (Vazza et al., in prep.).

Figures 5 and 6 give examples of the turbulent velocity field calculated with both the standard and local velocity methods, showing the same galaxy cluster in both cases, but in one case simulated with the signal–velocity variant of the viscosity, and in the other with the new time-dependent low–viscosity scheme. Note that we here selected a situation where a large (ca. 500 kpc long) laminar flow pattern can be easily identified close to the centre of one of our simulated clusters (*g72*). When the mean cluster velocity field is subtracted as in Figure 5, large residual bulk flow patterns remain visible, caused by a substructure moving through the cluster atmosphere. We colour-coded the turbulent kinetic energy of particles, $E_t(\boldsymbol{x}) \sim 1/2\,\rho(\boldsymbol{x})\sigma_v(\boldsymbol{x})^2$, after subtracting the local mean velocity field (here smoothed onto a $64^3$ mesh) for the up-

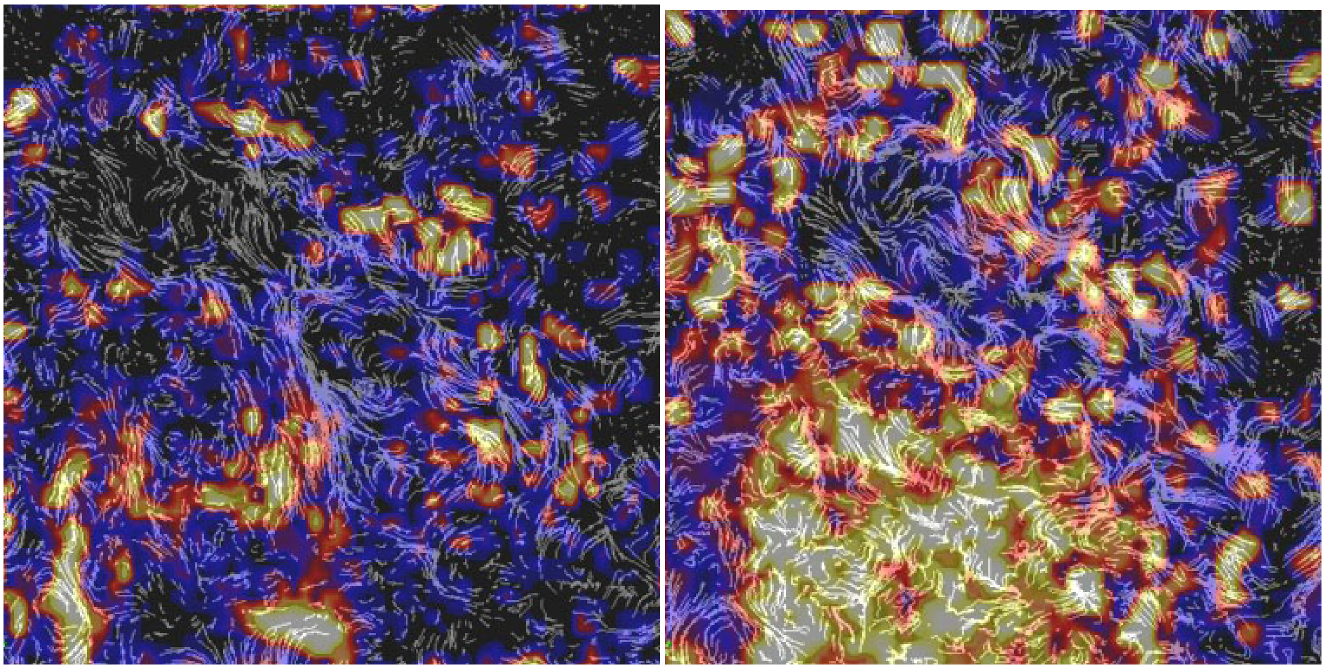

**Figure 6.** Same slice of the Gas velocity field as in figure 5 of cluster *g72* after subtracting the *local* mean velocity of the cluster. The panel on the left is for a run with the original viscosity of SPH while the panel on the right shows the result for the low viscosity scheme.

per panels and aster subtracting the *global* mean bulk velocity of the cluster for the lower panels. One can see that fluid instabilities of Kelvin-Helmholtz type are growing along the interfaces of the large laminar flow pattern, visible in the upper left panel. As expected, the strength of this turbulent velocity field is considerably larger in the simulation obtained with the new low–viscosity scheme, providing evidence that such instabilities are less strongly damped in this scheme. This can also be seen by the longer flow field lines in Figure 6. Figures 5 also visually confirms the differences in the two approaches of filtering the velocity field. Whereas the local–velocity approach highlights the energy within the velocity structure along boundary layers, the energy within the large, bulk motions are preferentially selected when only subtraction the *global* mean bulk velocity.

The total cumulative kinetic energy in the random gas motions inside our mesh (cantered on the cluster centre) reaches 5%-30% of the thermal energy for the simulations using the new, low–viscosity scheme, whereas it stays at much lower levels (≈2%-10%) when the signal velocity parameterisation of the viscosity is used. If the original viscosity scheme is used, it is typically at even lower values (≈1%-5%).

In general, we find that more massive clusters tend to have a higher fraction of turbulent energy content. However, given that our simulations have fixed mass resolution, this trend could in principle simply reflect a numerical resolution effect. In order to get further information on this, we have re-simulated one of the smaller clusters (*g676*) with 6 times better mass resolution using the signal velocity parameterisation of the viscosity. At $z = 0$, this cluster is then resolved by nearly as many particles as the massive clusters simulated with our standard resolution. We find that for this high-resolution simulation the level of turbulence ($\approx$ 3%) is increased compared with the normal resolution ($\approx$ 2%), but it stays less to what we found for the low–viscosity scheme at our normal resolution ($\approx$ 5%). This confirms two expectations. First, the low viscosity scheme effectively increases the resolution on which SPH simulations can resolve small-scale velocity structure, which otherwise gets already suppressed on scales larger than the smoothing length by spurious viscous damping effects due to the artificial viscosity. Second, the amount of turbulence in the high resolution version of *g676* is still less than what we find with the same viscosity implementation in the larger systems, and even much smaller than what we find with the low–viscosity scheme in the large clusters. This tentatively suggests that the trend of a mass-dependence of the importance of turbulence is not caused by numerical effects. Note that with a fixed physical scale of $1\,\mathrm{Mpc}$ we are sampling different fractions of $R_{\rm vir}$ in clusters of different masses. However, if, in case of the less massive system, we restrict the sampling relative to $R_{\rm vir}$ to measure within comparable volumes, the fraction of turbulent energy content found in the small cluster increase roughly by a factor of two. Thereby we still find a significant trend with mass when measuring turbulence within a fixed fraction of $R_{\rm vir}$. Although it should be mentioned, that unless the dissipation of turbulence on small scales will me modeled correctly in a physical granted way, the different formation time scales of systems with different masses can potentially also contribute to such a trend.

In order to verify that our method for measuring the local velocity dispersion gives reasonable values, Figure 7 shows a radial profile of the volume-weighted, relative difference between thermal pressure for the signal velocity based and low–viscosity run. Here we used the an average over the three massive clusters (*g1*,*g51* and *g72*) which have comparable masses. The solid line shows the relative difference in radial shells and indicates that the turbulent pressure support can reach even up to 50% in the central part and drops to 0 at approximately 0.2 $R_{\rm vir}$. The dashed line shows the cumulative difference, which over the total cluster volume contributes between 2% and 5% to the total pressure. The diamonds mark the measurement inferred from the local velocity dispersion within centred boxes of various sizes. We also calculate the difference between the signal velocity based and low–viscosity runs using the mean values over the three clusters. Qualitatively, there

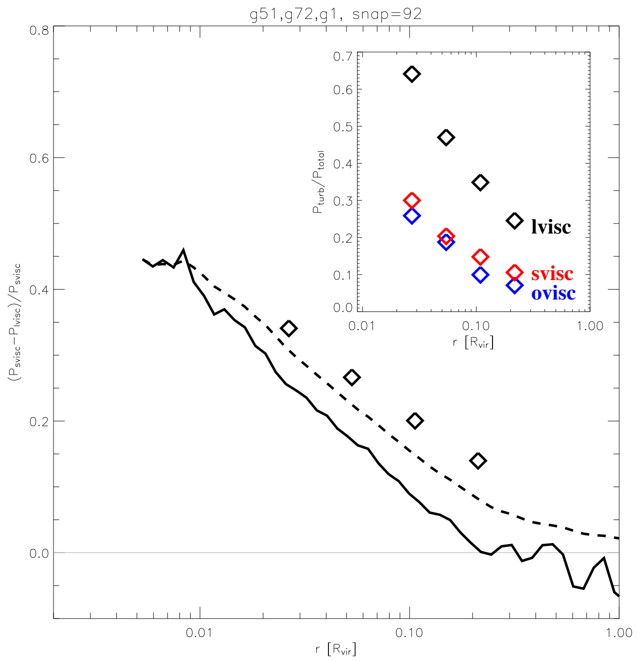


**Figure 7.** Radial profile of the relative thermal pressure difference averaged over three nearly equally massive clusters (*g1*,*g51* and *g72*), comparing the signal velocity based and low–viscosity runs (lines). The dashed line is the cumulative difference, whereas the solid line marks the profile in radial shells. The diamonds mark the difference in the turbulent energy support we inferred from the local velocity dispersion within several concentric cubes of different sizes ($l_{\rm cube} = 2r$) for the same runs. This should be compared with the dashed line. The inlay shows the absolute value inferred from the local velocity dispersion from the different viscosity parameterisations, respectively.

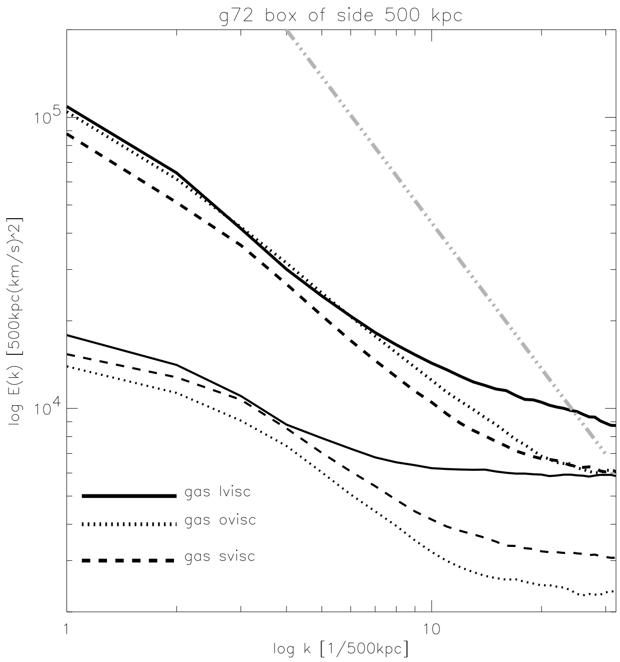


**Figure 8.** The energy spectra of the standard velocity fluctuations (*upper curves*) and of the local velocity fluctuations (*lower curves*) of gas particles in the central $500^3\mathrm{kpc}^3$ region of a cluster simulated with the original recipe for the artificial viscosity, with signal–velocity and with the low viscosity implementation. Additionally a Kolmogorov slope (dot-dot-dashed) is drawn for comparison.

is good agreement of results obtained with this approach with the cumulative curve. This confirms that our method to infer the turbulent energy content from the local velocity dispersion of the gas is meaningful. Note that the temperature which is used to calculate the pressure is determined by strong shock heating. As different resimulations of the same object can lead to small (but in this context non-negligible) timing differences, this can introduce sizable variations in the calculated pressure, especially during merging events. We verified that these differences for individual clusters are significantly larger than the differences between the cumulative curve (dashed line) and the data points from the local velocity dispersion (diamonds). Therefore we can only say that the two methods agree well within their uncertainties.

Finally, the inlay of Figure 7 gives the absolute contribution from the low–viscosity, the original viscosity in its two variants using the local velocity dispersion respectively. It seems that using the signal based viscosity in general leads already to more turbulence than the "old" original viscosity, but the time-dependent treatment of the viscosity works even more efficiently.

Although we are using a formalism which is suitable only for isotropic and homogeneous turbulence, the study of the turbulent energy spectrum may provide some useful insight. In the local mean velocity approach, we can obtain the diagonal part of the turbulent energy spectrum using Equation (13), with $R_{ii}$ approximated as

$$R_{ii}(r) = \langle [v_{a,i} - \overline{v}_i(\boldsymbol{x}_a)]\, [v_{b,i} - \overline{v}_i(\boldsymbol{x}_b)] \rangle_{\rm box}\,, \qquad (19)$$

where $\overline{\boldsymbol{v}}(\boldsymbol{x}_a)$ is the TSC–mean velocity of the cell which contains the point $\boldsymbol{x}_a$, and the average is over all pairs $(a, b)$ in the box with a certain distance $r$. In the standard approach, we would here subtract the centre-of-mass velocity of the cluster instead.

A major problem for estimating the correlation functions $R_{ii}(r)$ in this way, and with the energy spectrum calculated from SPH simulations (and in general from adaptive resolution approaches), is given by the non–uniform sampling of the point masses in the simulated box. To reduce this problem we focus on regions corresponding to the cores of galaxy clusters. Here the requirement of isotropic and homogeneous turbulence is hopefully better full filled. Also the density profile is relatively flat such that the sampling with gas particles is not too non-uniform. In addition, we estimate the correlation function as an average of dozens of Monte–Carlo extractions of gas particles from the simulated output, where we picked one particle from each of the $(15.6\,\mathrm{kpc})^3$ cells in order to have a uniform, volume-weighted set of particles.

In Figure 8, we show examples for the energy spectra we obtained for the two approaches by Fourier-transforming the measurements for $R_{ii}(r)$. The energy spectra for the two methods for treating the mean velocities are reasonably similar in shape, but the spectrum calculated with the local mean velocity has a lower normalisation, independent of resolution. This is expected because the TSC smoothing filters out contributions from laminar motions, and may also damp the turbulent field at some level. Both spectra show a slope nearly as steep as a Kolmogorov spectrum (which has $E(k) \propto k^{-5/3}$) at intermediate scales, but exhibit a significant flattening at smaller scales (i.e. large $k$). The flattening at small scales could be caused by numerical effects inherent in the SPH technique, where an efficient energy transfer to small-scale turbulent cells on scales approaching the numerical resolution is prevented, and thus a complete cascade cannot develop. Additional, the lack of numerical viscosity in the low–viscosity scheme can in principle lead to an increase of the noise level within the velocity field representation by the SPH particles on scales below the smoothing length. Such noise in general could contribute to the flattening at small scales. It is however not clear how to separate this noise component from a turbulent cascade reaching scales similar or below the smoothing length. Therefore one focus of future investigations has clearly be towards this issue. It is however important to note that the largest turbulent energy content (expecially at small scales) is always found in the clusters simulated with the low–viscosity scheme. This is particularly apparent in the energy spectra when the local velocity approach is used and suggests that the energy spectrum obtained with the standard approach is significantly affected by laminar bulk–flows, which are not sensitive to a change in parameterisation of the artifical viscosity.

## 6 CLUSTER PROPERTIES

Different levels of small-scale random gas motions within the ICM have only mild effects on global properties of clusters like mass or temperature, as evidenced by the measurements in Table 1. However, additional kinetic energy in turbulent motions changes the central density and entropy structure, which in turn has a sizable effect on the X-ray luminosity. We investigate the resulting changes in cluster scaling relations and radial profiles in more detail within this section.

### 6.1 Maps

The presence of a significant turbulent energy component in the intra-cluster medium manifests itself in a modification of the balance between the gravitational potential and the gas pressure. There are in fact observational reports that claim to have detected such fluctuations in pressure maps derived from X-ray observations (Schuecker et al. 2004). We here calculate artificial pressure $P_{\rm art}$ maps for our simulations, based on surface brightness maps ($L_x$) and spectroscopic-like (Mazzotta et al. 2004) temperature ($T_{sl}$) maps. This allows artificial pressure maps to be estimated as

$$P_{\rm art} = n\,T_{sl}, \tag{20}$$

where we defined

$$n = \left(L_x/\sqrt{T_{sl}}\right)^{\frac{1}{2}}. \tag{21}$$

Figures 9 and 10 show a comparison of a number of cluster maps produced using an unsharp-mask technique of the form

$$\mathrm{Image}_{\rm unsharpmask} = \mathrm{Image} - \mathrm{Smoothed}(\mathrm{Image}, \sigma), \tag{22}$$

where a Gaussian smoothing with FWHM of $\sigma = 200$ kpc was applied. We analyse maps of the X-ray surface brightness, spectroscopic-like temperature, 'true' pressure maps (e.g. based on Compton $y$) and artificial pressure maps constructed as described above. All maps show the central 2 Mpc of the cluster run *g1*, simulated with the low–viscosity scheme (right panels) compared with the original SPH scheme (left panels).

Disregarding the large contribution by substructure in all the X-ray related maps (therefore also in the artificial pressure map), all types of maps show clear signs of turbulence. It is noticeable in both runs, but it has a much larger extent and intensity in the the low–viscosity run. Note in particular the turbulent motions (appearing as lumpiness in the unsharp-mask images) in the wake of infalling substructures, and the earlier break-up of fluid interfaces when the new, reduced viscosity scheme is used.

Pressure maps (and therefore SZ maps) are arguably the most promising type of map when searching for observational imprints of turbulence. Apart from reflecting the large scale shape of the cluster they are known to be relatively featureless, because most of the substructures in clusters are in pressure equilibrium with their local surroundings, making them in principle invisible in pressure maps. On the other hand, the contribution of the turbulent motion to the local pressure balance can be expected to leave visible fluctuations in the thermal pressure map. This can indeed be seen nicely in the pressure (e.g. SZ) maps in Figure 10. Note that the amplitudes of the turbulent fluctuations in the case of the low–viscosity run are larger and also spatially more extended in the core of the cluster. Artificial pressure maps constructed from the X-ray observables still show such fluctuations, but they are partially swamped by the signatures of the infalling substructures, making it difficult to quantify the amount of turbulence present in clusters using such X-ray based artificial pressure maps.

The small displacements seen in the substructure positions between the two runs are due to small differences in their orbital phases. Besides the general problem to precisely synchronise cluster simulations with different dynamical processes involved, it is well known (e.g. Tormen et al. 2004; Puchwein et al. 2005) that the interaction of the gas with its environment can significantly change the orbits of infalling substructure. The different efficiencies in stripping the gas from the infalling substructure in the simulations with different viscosity prescription can therefore lead to small differences in the timing and orbits between the two simulations.

### 6.2 Scaling Relations

In Figure 11, we compare the mass-weighted temperature of our galaxy clusters for simulations with the original viscosity and for runs with the low–viscosity scheme. There are no significant changes. Comparing the X-ray luminosity instead, we find that it drops significantly by a factor of $\approx 2$ for clusters simulated with the low–viscosity scheme, as shown in Figure 12. This is quite interesting in the context of the long-standing problem of trying to reproduce the observed cluster scaling relations in simulations. In particular, since non radiative cluster simulations tend to produce an excess of X-ray luminosity, this effect would help. However, one has to keep in mind that the inclusion of additional physical processes like radiative cooling and feedback from star formation can have an even larger impact on the cluster luminosity, depending on cluster mass, so a definite assessment of the scaling relation issue has to await simulations that also include these effects.

### 6.3 Radial profiles

The presence of turbulence manifests itself in an increase of the velocity dispersion of the cluster gas, especially towards the centre, while the dark matter velocity dispersion should be unaffected. In Figure 13, we compare the velocity dispersion of gas and dark matter, averaged over the low- and high-mass clusters in our set. As expected, the velocity dispersion of the dark matter does not change in the low–viscosity simulations, where a larger degree of turbulence is present in the ICM. On the other hand, the central velocity dispersion of the gas increases, reaching of order of $400\,\mathrm{km\,s^{-1}}$ for our massive clusters. As the gas is in pressure equilibrium with the

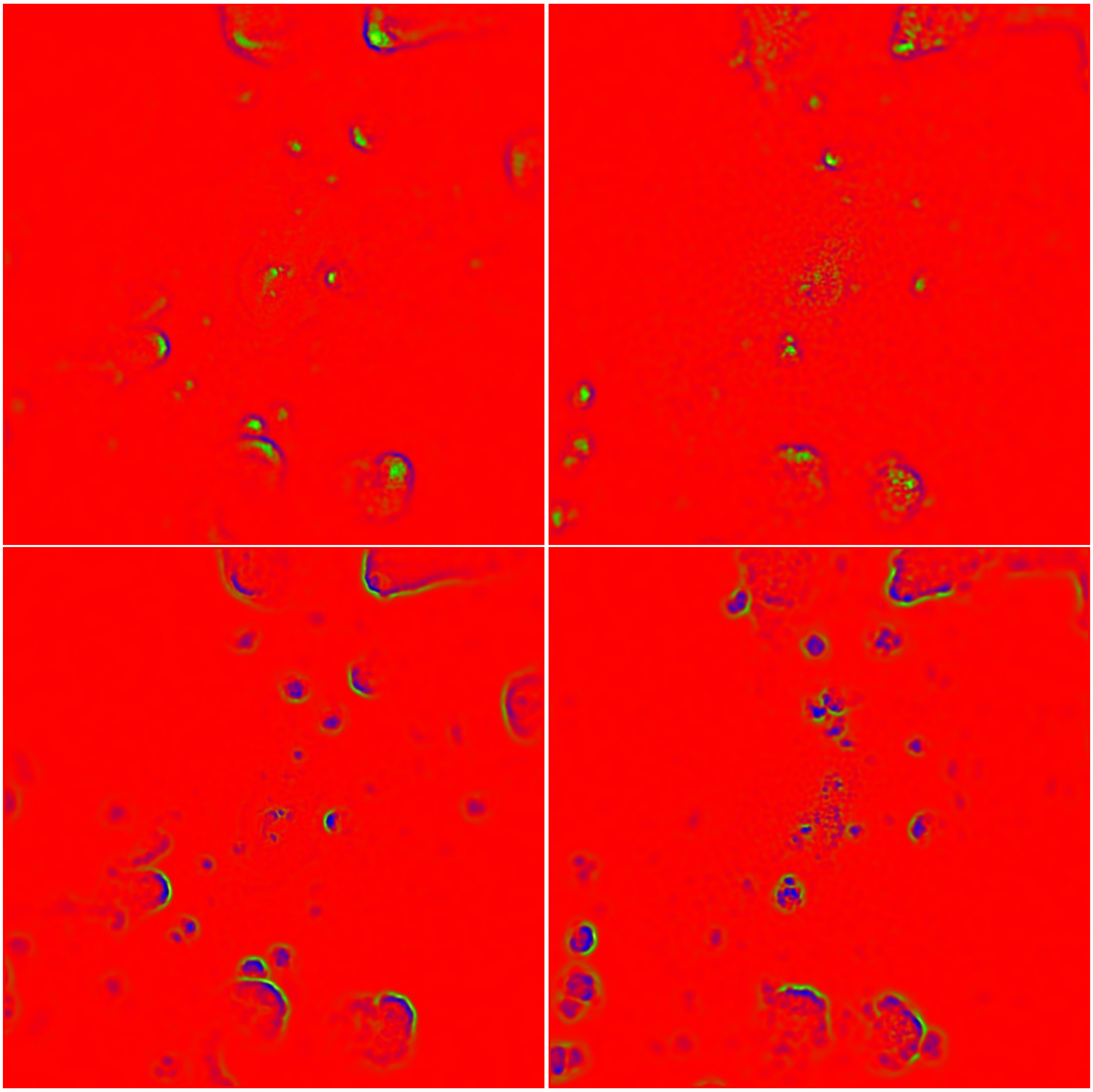

**Figure 9.** Unsharp mask images of X-ray maps for one of the massive clusters (*g1*), comparing runs with the low–viscosity scheme (right panels) with the original SPH scheme (left panels). The top row gives maps of surface brightness, while the bottom one compares maps of the 'spectroscopic like' temperature, both within 2 Mpc centred on the cluster. We can see evidence for an increased level of turbulent motions behind the infalling substructures, and a break-up of fluid interfaces for the reduced viscosity scheme is clearly visible. Also, there is a general increase of turbulence (appearing as lumpiness) towards the centre. However, the most prominent signals in the map stem from the higher density or different temperature of substructures relative to their surrounding, or from shocks and contact discontinuities. For this reason, turbulence can be better identified in pressure maps (see Figure 10).

unchanged gravitational potential, the hydrodynamic gas pressure will be correspondingly lower in the centre due to the presence of these random gas motions.

In Figure 15, we show the mean cluster temperature profiles, which only shows a very mild trend of increasing temperature in the central part of clusters when using the new, low–viscosity scheme. However, the central gas density drops significantly in the low–viscosity scheme, as shown in Figure 14. This change in density is restricted to inner parts of the cluster, roughly to within $0.1R_{vir}$, which may be taken as an indication of the size of the region where turbulent motions are important.

Quite interestingly, the presence of turbulence also changes the entropy profiles. In Figure 16, we show the radial entropy profiles of our clusters, which in the case of the low–viscosity scheme exhibit an elevated level of entropy in the core, with a flattening similar to that inferred from X-ray observations. It is remarkable that this central increase of entropy occurs despite the fact that the source of entropy generation, the artificial viscosity, is in princi-

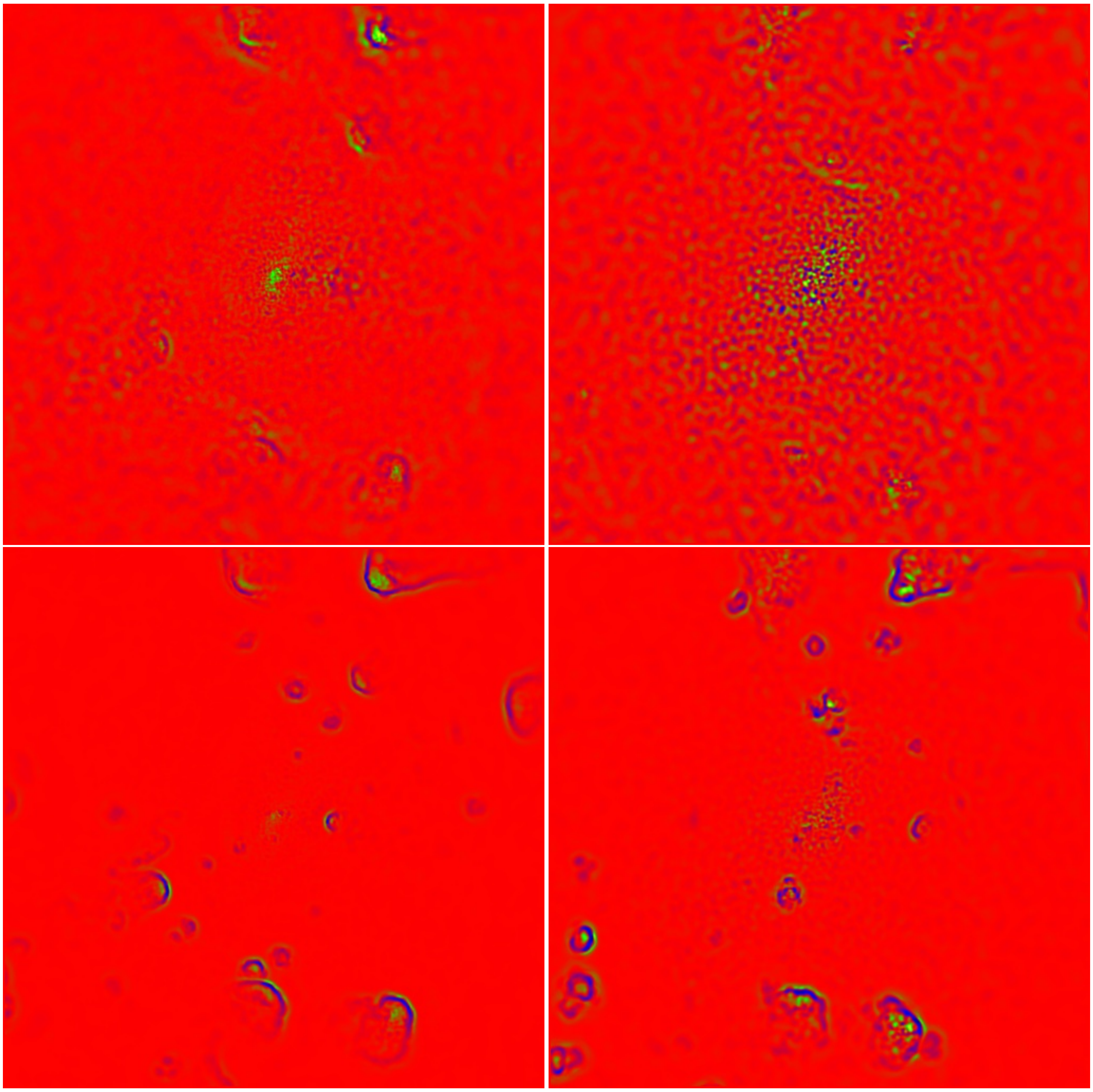

**Figure 10.** Unsharp mask images of pressure maps of one of the massive clusters (*g1*), comparing runs with the low–viscosity scheme (right panels) with the original SPH scheme (left panels). We also compare different methods for determining the pressure maps. The panels of the top row show Compton-$y$ maps (which can be associated with projected, thermal pressure maps), whereas the maps in the bottom row are pressure maps derived based on X-ray surface brightness and spectroscopic temperature maps, see equation 20 and 21. Both kinds of maps show an increase of structure (lumpiness) for the simulation which uses the reduced viscosity scheme (right panels) when compared with the original SPH viscosity scheme (left panels). The maps based on X-ray observables show a larger degree of lumpiness due to the gas around substructures, especially in the vicinity of infalling subgroups.

ple less efficient in the low–viscosity scheme. There are two main possibilities that could explain this result. Either the low–viscosity scheme allows shocks to penetrate deeper into the core of the cluster and its progenitors such that more efficient entropy production in shocks occurs there, or alternatively, the reduced numerical viscosity changes the mixing processes of infalling material, allowing higher entropy material that falls in late to end up near the cluster centre.

In order to investigate a possible change of the accretion behaviour, we traced back to high redshift all particles that end up at $z = 0$ within 5% of $R_{\rm vir}$ of the cluster centre. We find that most of the central material is located in the centres of progenitor halos at higher redshift, which is a well known result. However, in the simulations with the time dependend, low–viscosity scheme, there is a clear increase of the number of particles which are not associated with the core of a halo at higher redshift. We illustrate this with the histograms shown in Figure 17, which gives the distribution of the distance to the nearest halo in units of $R_{\rm vir}$ of the halo.

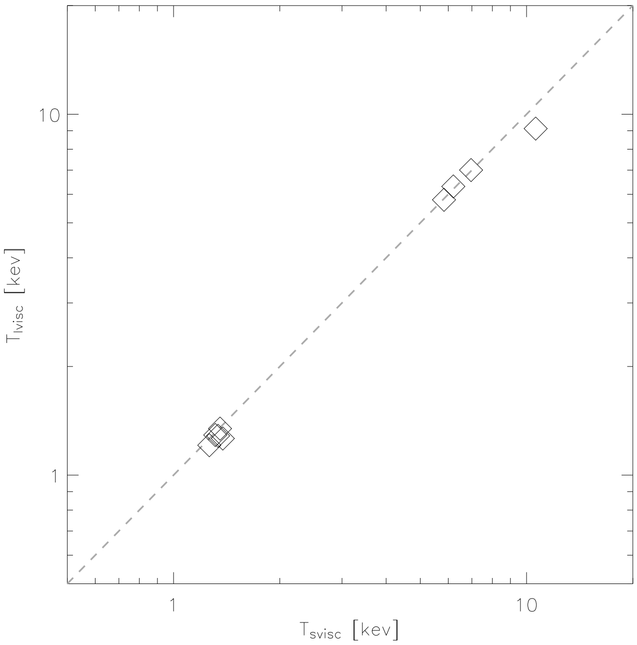


**Figure 11.** Comparison of the virial temperature of the 9 clusters when different parameterisations of the viscosity are employed. The solid line marks the one-to-one correspondence.

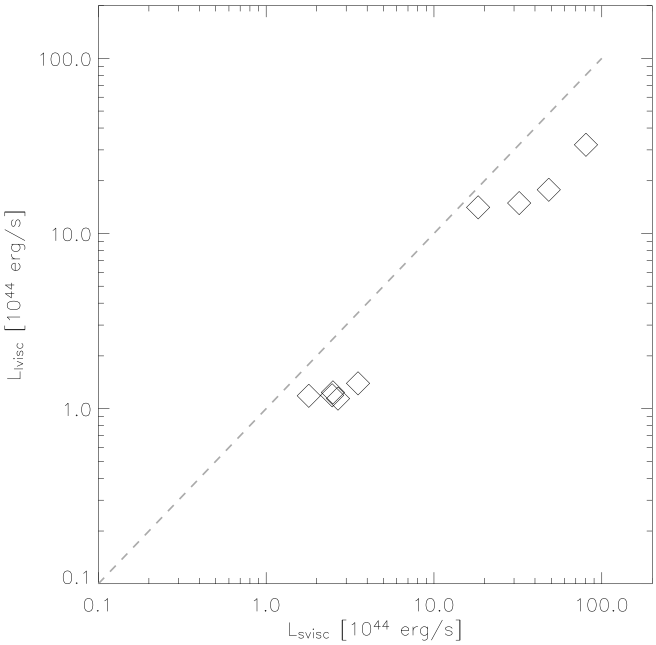


**Figure 12.** Comparison of the bolometric luminosity of the 9 clusters when different parameterisations of the viscosity are employed. The solid line marks the one-to-one correspondence. It is evident that clusters with a larger degree of turbulence have a lower luminosity.

All particles at distances larger than 1 are not associated with any halo at corresponding epoch. Compared to the low entropy material that is already bound in a dense core at this epoch, this diffuse gas is brought to much higher entropy by shocks. When it is later accreted onto the cluster and mixed into the core, it can then raise the entropy level observed there. We note that Eulerian hydrodynamics simulations also show a flattening of the entropy profile. While the exact degree to which numerical and physical (turbulent) mixing contribute to producing this result is still a matter of debate, it is intriguing that a larger level of turbulence in the SPH calculations substantially alleviates the discrepancies in the results otherwise obtained with the two techniques (Frenk et al. 1999; O'Shea et al. 2003).

## 7 METAL LINES

Turbulent gas motions can lead to substantial Doppler broadening of X-ray metal lines, in excess of their intrinsic line widths. Given the exquisite spectral resolution of upcoming observational X-ray mission, this could be used to directly measure the degree of ICM turbulence (Sunyaev et al. 2003) by measuring, e.g., the shape of the $6.702\,\mathrm{keV}$ iron emission line.

One potential difficulty in this is that multiple large-scale bulk motions of substructure moving inside the galaxy cluster along the line of sight might dominate the signal. To get a handle on this, we estimate the line-of-sight emission of the $6.702\,\mathrm{keV}$ iron line within columns through the simulated clusters, where the column size was chosen to be $300\,h^{-1}\mathrm{kpc}$ on a side, which at the distance of the Coma cluster corresponds roughly to one arcmin, the formal resolution of ASTRO-E2. For simplicity, we assign every gas particle a constant iron abundance and an emissivity proportional to $n_e^2 \times f(T_e) \times \Delta V$, where $n_e$ is the electron density, and $\Delta V \propto \rho^{-1}$ is the volume represented by the particle. As a further approxima-

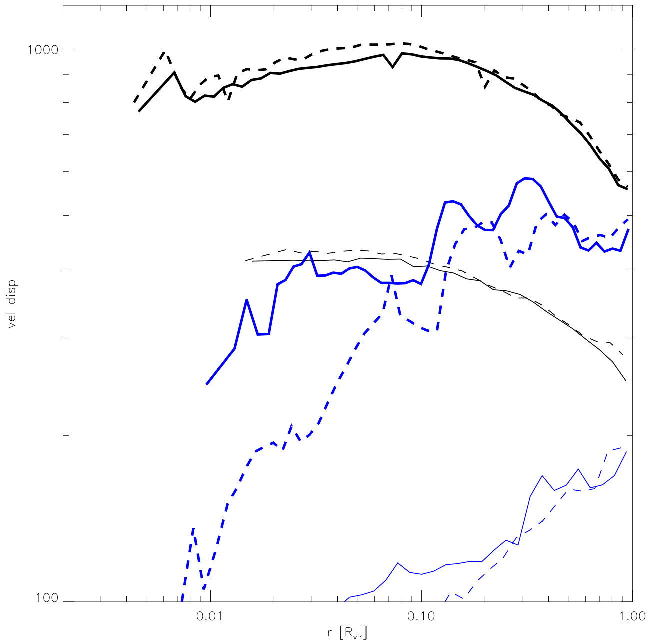


**Figure 13.** Radial velocity dispersion profile for dark matter (black) and gas (blue) particles. The thick lines represent the average over the 4 massive clusters, whereas the thin lines give the average over the 5 low mass systems. The dashed lines are drawn from the original viscosity simulations, the solid lines from the low–viscosity simulations.

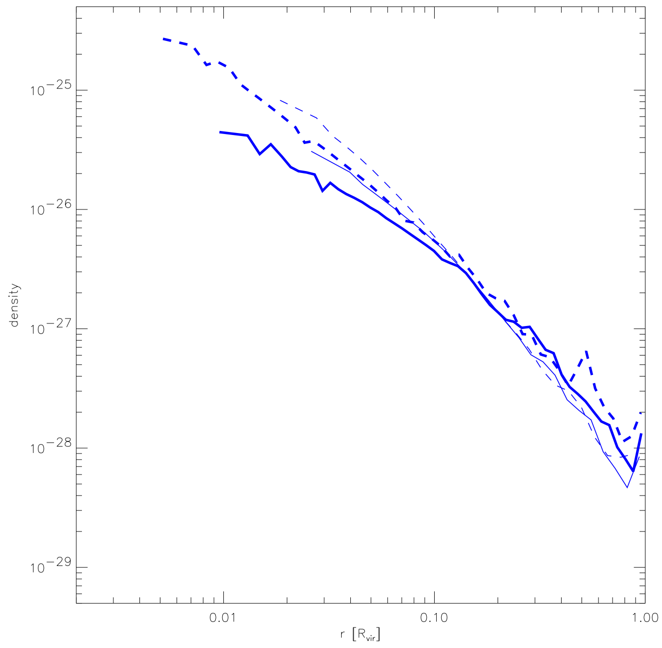


**Figure 14.** Radial gas density profile. The thick lines represent the average over the 4 massive clusters, whereas the thin lines give the average over the 5 low mass systems. The dashed lines are drawn from the original viscosity simulations, the solid lines from the low–viscosity simulations.

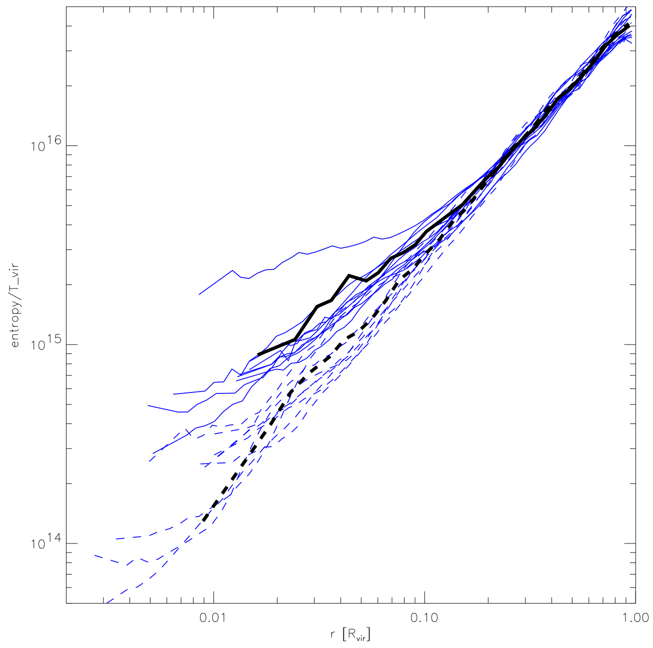


**Figure 16.** Radial entropy profiles of the ICM gas. Thin lines are individual profiles for the 9 clusters, thick lines are averages. The dashed lines are drawn from the original viscosity simulations, the solid lines from the low–viscosity simulations.

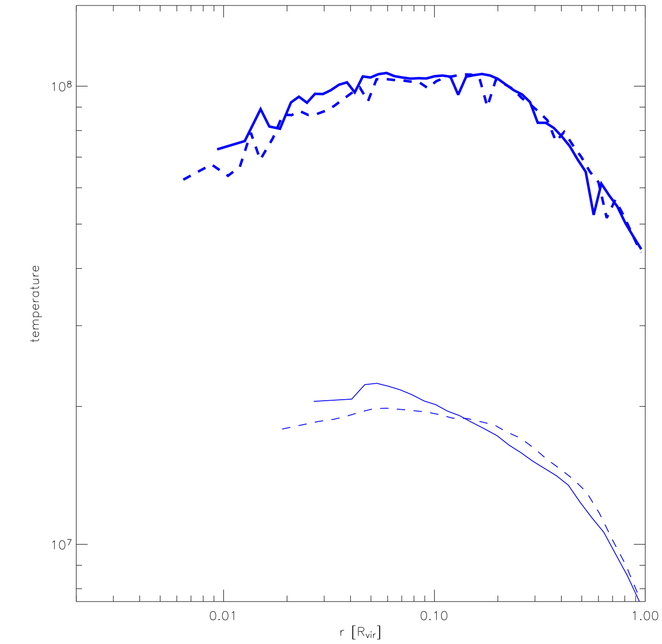


**Figure 15.** Mass-weighted gas temperature profile. The thick lines represent the average over the 4 massive clusters, whereas the thin lines give the average over the 5 low mass systems. The dashed lines are drawn from the original viscosity simulations, the solid lines from the low–viscosity simulations.

tion we set the electron abundance equal to unity. We also neglect thermal broadening and other close lines (like the $6.685\,\mathrm{keV}$ iron line), given that the $6.702\,\mathrm{keV}$ iron line is clearly the strongest.

In Figure 18, we show the resulting distributions for several lines of sight, here distributed on a grid with $-500$, $-250$, 0, 250 and 500 $h^{-1}\mathrm{kpc}$ impact parameter in $x$-direction, and $-250$, 0 and 250, $h^{-1}\mathrm{kpc}$ impact parameter in the $y$-direction, respectively. The different lines in each panel correspond to simulations with the signal-velocity based viscosity (dashed line) and with the time-depended low–viscosity scheme (solid lines). Both results have been normalised to the total cluster luminosity, such that the integral under the curves corresponds to the fraction of the total luminosity.

We note that this measurement is very sensitive to small timing differences between different simulations, and therefore a comparison of the same cluster run with different viscosity should be carried out in a statistical fashion, even if some features look very similar in both runs. In general we confirm previous findings (e.g. Inogamov & Sunyaev 2003) that large bulk motions can lead to spectral features which are several times wider than expected based on thermal broadening alone. Additional complexity is added by beam smearing effects, thermal broadening, and by the local turbulence in the ICM gas, such that an overall very complex line shape results. In our simulations with the low–viscosity scheme, where we have found an increased level of fluid turbulence, the final line shapes are indeed more washed out. However, the complexity of the final line shapes suggests that it will be very difficult to accurately measure the level of fluid turbulence with high resolution spectra of X-ray emission lines, primarily because of the confusing influence of large-scale bulk motions within galaxy clusters.

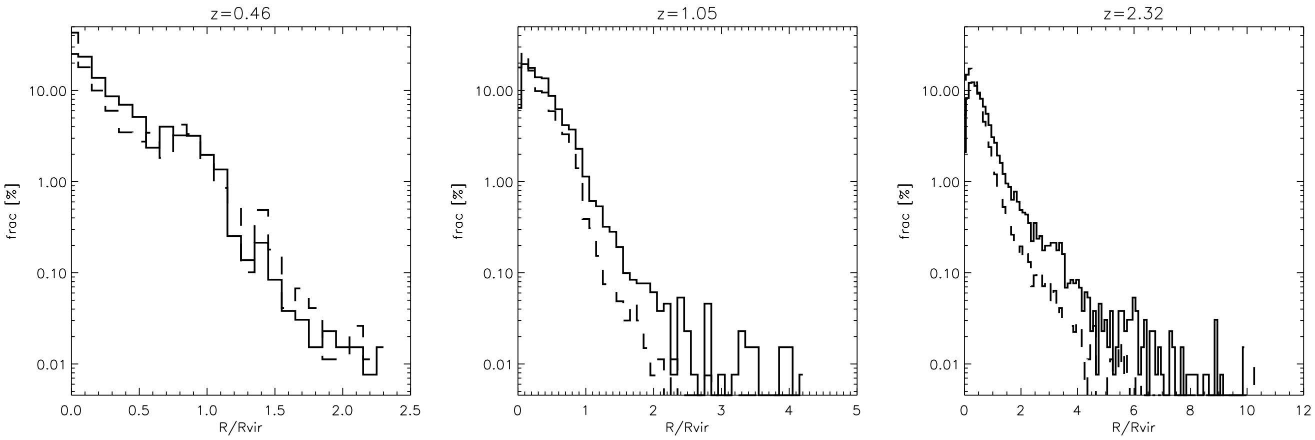


**Figure 17.** Distribution of the distance of particles to their nearest halo at high redshift. The particles selected here end up within 5% of $R_{\rm vir}$ at $z = 0$. The dashed lines are for the original viscosity scheme, while the solid lines mark the result for the low–viscosity simulations.

## 8 APPLICATION TO RADIO HALOS

One promising possibility to explain the extended radio emission on Mpc-scales observed in a growing number of galaxy clusters is to attribute it to electron acceleration by cluster turbulence (e.g., Schlickeiser et al. 1987; Brunetti et al. 2001). Having high resolution cluster simulations at hand, which thanks to the new viscosity scheme are able to develop significant turbulence within the ICM, it is of interest to explore this possibility here. Obviously, due to the uncertainties in the complex physical processes of dissipation of the turbulent energy – which up to this point can not be explicitly modelled in the simulations – our analysis is limited to a check whether or not turbulent reacceleration can plausibly reproduce some of the main properties of radio halos. In this scenario, the efficiency of electron acceleration depends on the energy density of magnetohydrodynamic waves (Alfvén waves, Fast Mode waves, …), on their energy spectrum, and on the physical conditions in the ICM (i.e., density and temperature of the thermal plasma, strength of the magnetic field in the ICM, number density and spectrum of cosmic rays in the ICM). A number of approaches for studying the acceleration of relativistic electrons in the ICM have been successfully developed by focusing on the case of Alfvén waves (Ohno et al. 2002; Brunetti et al. 2004) and, more recently, on Fast Mode-waves (Cassano & Brunetti 2005).

It should be stressed, however, that analytical and/or semi–analytical computations are limited to very simple assumptions for the generation of turbulence in the ICM. Full numerical simulations represent an ideal complementary tool for a more general analysis, where the injection of turbulence into the cluster volume by hierarchical merging processes can be studied realistically. Low numerical viscosity and high spatial resolution are however a prerequisite for reliable estimates of turbulence. As we have seen earlier, previous SPH simulations based on original viscosity parameterisations have suppressed random gas motions quite strongly, but the low–viscosity scheme explored here does substantially better in this respect.

In this Section, we carry out a first exploratory analysis of the efficiency of electron acceleration derived in the low–viscosity scheme, and we compare it to results obtained with a original SPH formulation. For definiteness, we assume that a fraction $\eta_t$ of the estimated energy content of the turbulent velocity fields in the cluster volume, measured by the local velocity dispersion (equation 16, section 5), is in the form of Fast Mode waves. We focus on these modes since relativistic electrons are mainly accelerated by coupling with large scale modes (e.g., $k^{-1} \geqslant$ kpc, $k$ being the wave number) whose energy density, under the above assumption, can hopefully be constrained with the numerical simulations in a reliable fashion. In addition, the damping and time evolution of Fast Modes basically depend only on the properties of the thermal plasma and are essentially not sensitive to the presence of cosmic ray protons in the ICM (Cassano & Brunetti 2005).

Relativistic particles couple with Fast Modes via magnetic Landau damping. The necessary condition for Landau damping (Melrose 1968; Eilek 1979) is $\omega - k_{\parallel} v_{\parallel} = 0$, where $\omega$ is the frequency of the wave, $k_{\parallel}$ is the wavenumber projected along the magnetic field, and $v_{\parallel} = v\mu$ is the projected electron velocity. Note that in this case - in contrary to the Alfvénic case - particles may also interact with large scale modes. In the collisionless regime, it can be shown that the resulting acceleration rate in an isotropic plasma (modes' propagation and particle momenta) is given by (e.g., Cassano & Brunetti 2005)

$$\frac{{\rm d}p}{{\rm d}t} \sim 180\, \frac{v_{\rm M}^2}{c} \frac{p}{B^2} \int {\rm k} W_k^B {\rm d}k, \tag{23}$$

where $v_{\rm M}$ is the magneto–sonic velocity, and $W_k^B$ is the energy spectrum of the magnetic field fluctuations (e.g., Barnes & Scargle 1973; Cassano & Brunetti 2005). We estimate the rate of injection of Fast Modes, $I_k^{FM}$, assuming that a fraction, $\eta_t$, of fluid turbulence is associated with these modes. We parameterise the injection rate assuming that turbulence is injected (and also dissipated) in galaxy clusters within a time of the order of a cluster–crossing time, $\tau_{\rm cross}$ (see Cassano & Brunetti 2005; Subramanian et al. 2005,for a more detailed discussion). One then has:

$$\int I_k^{FM}\, {\rm d}k \sim \eta_t \frac{E_t}{\tau_{\rm cross}} \sim \frac{1}{2} \eta_t \rho_{\rm gas} \sigma_v^2 \tau_{\rm inject}^{-1} \tag{24}$$

Here, $\tau_{\rm inject}$ is the time over which a merging substructure is able to inject turbulence in a given volume element in the main cluster. This can be estimated as the size of the subhalo divided by its infalling velocity. As the size of a halo is only a weak function of its mass, we approximate $\tau_{\rm inject}$ with a generic value of $\tau_{\rm inject} = 0.5\,{\rm Gyr}$. This is only a very crude estimate and more generally one should think of an effective efficiency parameter $\eta_t^{\rm eff} = \eta_t / \tau_{\rm inject}$ which we set to $0.1/(0.5\,{\rm Gyr})$ as argued before. Note also that for estimating $\sigma_v^2$ we used a $64^3$ TSC-grid, which is a conservative

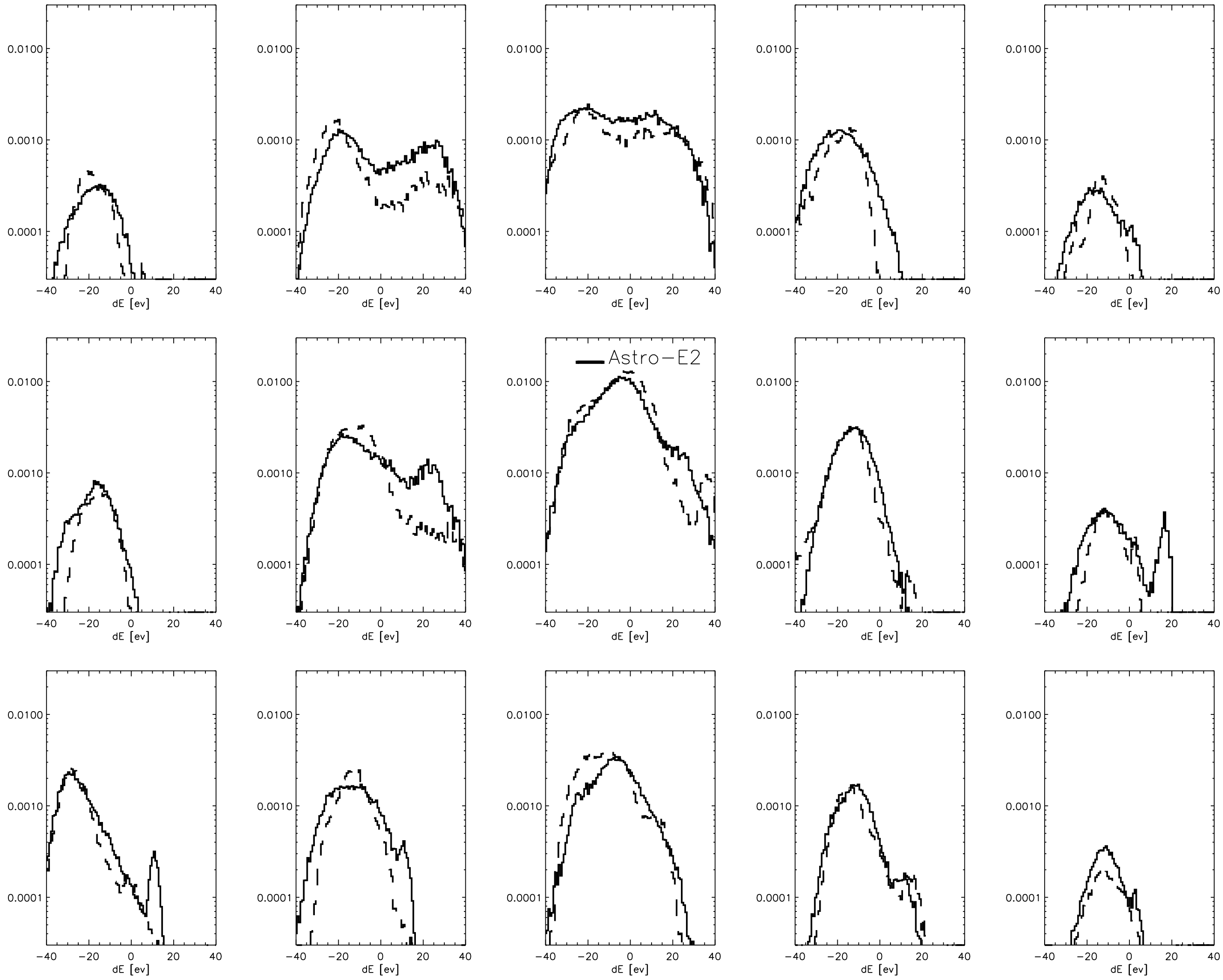


**Figure 18.** Distribution of the Doppler-shifted emission of the iron $6.702\,\mathrm{keV}$ line for 15 lines of sight through the cluster *g72*. Every panel corresponds to a column of side length $300\,h^{-1}\mathrm{kpc}$ through the virial region of the cluster. This roughly corresponds to one arcmin resolution (comparable to the ASTRO-E2 specifications) at the distance of the Coma cluster. The columns from left to right correspond to $-500$, $-250$, $0$, $250$, and $500\,h^{-1}\mathrm{kpc}$ impact parameter in the $x$-direction, and the rows correspond to $-250$, $0$, and $250$, $h^{-1}\mathrm{kpc}$ impact parameter in the $y$-direction. The dashed lines give results for the original viscosity run, while the solid line is for the low–viscosity run. The thick bar in the center panel marks the expected energy resolution of 12 eV of the XRS instrument on-board ASTRO-E2.

estimate, as shown in Figure 4, and therefore equation (24) should still reflect a lower limit.

Following Cassano & Brunetti (2005), the spectrum of the magnetic fluctuations associated with Fast Modes is computed under stationary conditions taking into account the damping rate of these modes with thermal electrons, $\Gamma_k = \Gamma_o k$. One then has

$$W_k^B \sim \frac{B_o^2}{8\pi}\frac{1}{P_{\rm gas}}\frac{I_k^{FM}}{\Gamma_o k}. \qquad (25)$$

Thus the integral in Eqn. (23) at each position of the grid can be readily estimated as

$$\int k W_k^B \,\mathrm{d}k \;\sim\; \frac{B_o^2}{8\pi}\frac{1}{\Gamma_o P_{\rm gas}}\int I_k^{FM}\,\mathrm{d}k \qquad (26)$$

$$\sim\; \eta_t^{\rm eff}\,\frac{B^2(\mathbf{x})}{16\pi}\,\frac{\rho_{\rm gas}(\mathbf{x})\sigma_{ii}^2(\mathbf{x})}{P_{\rm gas}(\mathbf{x})}\,\frac{1}{\Gamma_o} \qquad (27)$$

where $\Gamma_o$ depends on the temperature of the ICM (Cassano & Brunetti 2005)[1].

In this Section we are primarily interested in determining the maximum energy of accelerated electrons, given the adopted energy density for Fast Modes. Under typical conditions in the ICM, the maximum energy of electrons is reached at energies where radiative losses balance the effect of the acceleration. The radiative synchrotron and inverse Compton losses with CMB photons are given by (e.g., Sarazin 1999)

$$\left(\frac{\mathrm{d}p}{\mathrm{d}t}\right)_{\rm rad} = -4.8\times10^{-4}p^2\left[\left(\frac{B_{\mu G}}{3.2}\right)^2\frac{\sin^2\theta}{2/3}+(1+z)^4\right] = -\frac{\beta\,p^2}{m_e\,c}, \qquad (28)$$

[1] Note that under these assumptions the efficiency of the particle acceleration does not depend on the spectrum of the waves

where $B_{\mu G}$ is the magnetic field strength in $\mu G$, and $\theta$ is the pitch angle of the emitting electrons. If an efficient isotropisation of electron momenta can be assumed, it is possible to average over all possible pitch angles, so that $\left\langle \sin^2\theta \right\rangle = 2/3$.

In Figure 19, we plot the maximum energy of the fast electrons obtained from Eqs. (25) and (28) along one line-of-sight through the cluster atmosphere. The two different lines are for the same cluster, simulated with our two main schemes for the artificial viscosity. The two vertical lines in Figure 5 are indicating the position of these cuts. When the new low–viscosity scheme is used, enough turbulence is resolved to maintain high energy electrons (and thus synchrotron radio emission) almost everywhere out to a distance of 1 Mpc from the cluster centre, whereas in the original formulation of SPH, turbulence is much more strongly suppressed, so that the maximum energy of the accelerated electrons remains a factor of about three below that in the low–viscosity case.

The results reported in Figure 19 are obtained assuming a reference value of $\eta_t^{\rm eff} = \eta_t/\tau_{\rm inject} = 0.1/(0.5\,{\rm Gyr})$. The averaged volume weighted magnetic field strength in the considered cluster region is fixed at $0.5\mu G$ and a simple scaling from magnetic flux–freezing, $B \propto \rho^{(2/3)}$, is adopted in the calculations, resulting in a central magnetic field strength of $B_0 = 5.0\mu G$. It is worth noting that the maximum energy of the accelerated electrons, $\gamma_{\rm max}$, scales with the energy density of the turbulence (and with the fraction of the energy of this turbulence channelled into Fast Modes $\eta_t$, Eq. 25). However the synchrotron frequency emitted by these electrons scales with the square of the turbulent energy ($\gamma_{\rm max}^2$). Interestingly, with the parameter values adopted in Figure 19, a maximum synchrotron frequency of order $10^2(\eta_t/0.1)^2$ MHz is obtained in a Mpc–sized cluster region, which implies diffuse synchrotron radiation up to GHz frequencies if a slightly larger value of $\eta_t$ is adopted[2]. On the other hand, we note that essentially no significant radio emission would be predicted if we had used the simulations with the original SPH viscosity scheme.

In real galaxy clusters, the level of turbulence which can form will also depend on the amount of physical viscosity present in the ICM gas (i.e. on its Reynolds number), which in turn depends on the magnetic field topology and gas temperature. It will presumably still take a while before the simulations achieve sufficient resolution that the numerical viscosity is lower than this physical viscosity. In addition, the details of the conversion process of large–scale velocity fields into MHD modes is still poorly understood and well beyond the capabilities of presently available cosmological simulations. However, our results here show that a suitable modification of the artificial viscosity parameterisation within SPH can be of significant help in this respect, and it allows a first investigation of the role of turbulence for feeding non–thermal phenomena in galaxy clusters.

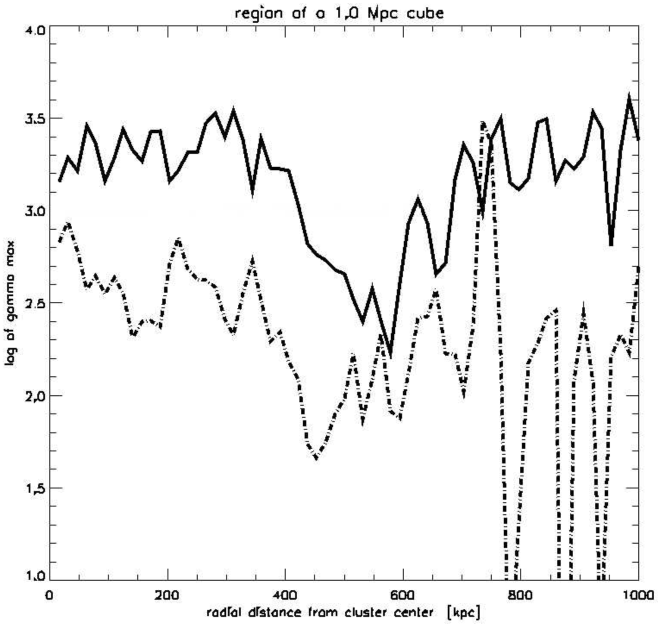


**Figure 19.** One-dimensional profile of the maximum energy of the electrons accelerated via the turbulent-magneto-sonic model, along the same vertical lines drawn in Figure 5. Dashed lines are for the original viscosity run, while solid lines are for the low–viscosity scheme. Here, a conservative $64^3$ grid is used in the TSC smoothing.

## 9 CONCLUSIONS

We implemented a new parameterisation of the artificial viscosity of SPH in the parallel cosmological simulation code GADGET-2. Following a suggestion by Morris & Monaghan (1997), this method amounts to an individual, time-dependent strength of the viscosity for each particle which increases in the vicinity of shocks and decays after passing through a shock. As a result, SPH should show much smaller numerical viscosity in regions away from strong shocks than original formulations. We applied this low–viscosity formulation of SPH to a number of test problems and to cosmological simulations of galaxy cluster formations, and compared the results to those obtained with the original SPH formulation. Our main results can be summarised as follows:

- The low–viscosity variant of SPH is able to capture strong shocks just as well as the original formulation, and in some cases we even obtained improved results due to a reduced broadening of shock fronts. In spherical accretion shocks, we also obtained slightly better results due to a reduction of pre-shock entropy generation.
- Using the low–viscosity scheme, simulated galaxy clusters developed significant levels of turbulent gas motions, driven by merger events and infall of substructure. We find that the kinetic energy associated with turbulent gas motion within the inner $\sim 1\,{\rm Mpc}$ of a $10^{15}\,h^{-1}{\rm M}_\odot$ galaxy cluster can be up to 30% of the thermal energy content. This value can be still larger and reach up to 50% in the very central part of massive clusters. In clusters with smaller masses ($\sim 10^{14}\,h^{-1}{\rm M}_\odot$) we find a smaller turbulent energy content, reaching only 5% within the central Mpc. Within a comparable fraction of the virial radius, the corresponding fraction is however still of order 10%. These values are much larger than what is found when the original SPH viscosity is employed, which strongly suppresses turbulent gas motions.
- The presence of such an amount of turbulence has an imprint on global properties of galaxy clusters, most notably reducing the bolometric X-ray luminosity in non radiative simulations by a factor of $\approx 2$. However, the global, mass-weighted temperature does not change.
- The temperature profiles of galaxy clusters are only mildly changed by the presence of turbulence, but we observe a strong decrease of density within the central region of galaxy clusters, where

[2] Note that (e.g., Cassano & Brunetti 2005) required $\eta_t \sim 0.2 - 0.3$ in order to reproduce the observed statistics of radio halos.

the turbulence is providing a significant contribution to the total pressure. Also the radial entropy profiles show a significant flattening towards the cluster centre. This makes them more similar to the observed profiles based on X-ray observations. Note however that radiative cooling – which was not included in our simulations – can also modify the profiles substantially. We find that the higher entropy in the centre found in the low viscosity simulations is largely a result of the more efficient transport and mixing of low-entropy in infalling material into the core of the cluster. We note that the elevated entropy levels found in our low–viscosity runs are more similar to the results found with Eulerian hydrodynamic codes than the original SPH ones.

• Turbulence in galaxy clusters broadens the shape of metal lines observable with high-resolution X-ray spectrographs like XRT on board of ASTRO-E2. Depending on the strength of the turbulence and the dynamical state of the cluster, prominent features due to large-scale bulk motions may however get washed out and blended into a very complex line structure. In general it will therefore be difficult to isolate the signature of the turbulent broadening and to differentiate it unambiguously from the more prominent features of large scale bulk motions.

• Applying a model for accelerating relativistic electrons by ICM turbulence we find that galaxy clusters simulated with reduced viscosity scheme may develop sufficient turbulence to account for the radio emission that is observed in many galaxy clusters, provided that a non–negligible fraction of the turbulent energy in the real ICM is associated with Fast Modes.

In summary, our results suggest that ICM turbulence might be an important ingredient in the physics of galaxy clusters. If present at the levels inferred from our low–viscosity simulations, it has a significant effect on the radial structure and on the scaling relations of galaxy clusters. We also note that the inferred reduction of the X-ray luminosity has a direct influence on the strength of radiative cooling flows. The more efficient mixing processes would also help to understand the nearly homogeneous metal content observed for large parts of the cluster interior. Finally, cluster turbulence may also play an important role for the dynamics of non-thermal processes in galaxy clusters.

Although we observe a rather high level of turbulence in the very centre of our simulated galaxy clusters when we use the low–viscosity scheme, it is likely that we are still missing turbulence due to the remaining numerical viscosity of our hydrodynamical scheme, and due to the resolution limitations, particularly in low density regions, of our simulations. This problem should in principle become less and less severe as the resolution of the simulations is increased in future calculations. However, given that there is a some physical viscosity in real galaxy clusters which limits the Reynolds number of the ICM, it cannot be the goal to model the ICM as a pure ideal gas. Instead, future work should concentrate on accurately characterising this physical viscosity of the ICM, which could then be directly incorporated into the simulations by means of the Navier-Stokes equations. Our results suggest that the low–viscosity formulation of SPH should be of significant help in reducing the numerical viscosity of SPH simulation below the level of this physical viscosity, and the present generation of simulations may already be close to this regime.

## ACKNOWLEDGEMENTS

Many thanks to Volker Springel for providing GADGET-2 and initial conditions for test problems. We acknowledge fruitful discussions with Stefano Borgani and want to thank Volker Springel and Torsten Ensslin for carefully reading and fruitful suggestions to improve the manuscript. The simulations were carried out on the IBM-SP4 machine at the "Centro Interuniversitario del Nord-Est per il Calcolo Elettronico" (CINECA, Bologna), with CPU time assigned under an INAF-CINECA grant, on the IBM-SP3 at the Italian Centre of Excellence "Science and Applications of Advanced Computational Paradigms", Padova and on the IBM-SP4 machine at the "Rechenzentrum der Max-Planck-Gesellschaft" in Garching. K. D. acknowledges support by a Marie Curie Fellowship of the European Community program "Human Potential" under contract number MCFI-2001-01227. G. B. acknowledges partial support from MIUR through grant PRIN2004 and from INAF through grant D4/03/15.

## REFERENCES


Balsara D. S., 1995, Journal of Computational Physics, 121, 357

Barnes A., Scargle J. D., 1973, ApJ, 184, 251

Bertschinger E., 1985, ApJS, 58, 1

Brunetti G., 2003, in Matter and Energy in Clusters of Galaxies, ASP Conference Proceedings, vol. 301, 349

Brunetti G., Blasi P., Cassano R., Gabici S., 2004, MNRAS, 350, 1174

Brunetti G., Setti G., Feretti L., Giovannini G., 2001, MNRAS, 320, 365

Buote D. A., 2001, ApJ, 553, L15

Cassano R., Brunetti G., 2005, MNRAS, 357, 1313

Choudhuri A. R., ed., 1998, The physics of fluids and plasmas : an introduction for astrophysicists /

Dolag K., Bartelmann M., Lesch H., 1999, ApP, 348, 351

Dolag K., Bartelmann M., Lesch H., 2002, ApP, 387, 383

Eilek J. A., 1979, ApJ, 230, 373

Feretti L., 2002, in IAU Symposium, 133

Feretti L., Gioia I. M., Giovannini G., 2002, Merging Processes in Galaxy Clusters, ASSL Vol. 272: Merging Processes in Galaxy Clusters

Frenk C. S., White S. D. M., Bode P., et al., 1999, ApJ, 525, 554

Fusco-Femiano R., Orlandini M., De Grandi S., et al., 2003, ApP, 398, 441

Giovannini G., Tordi M., Feretti L., 1999, New Astronomy, 4, 141

Inogamov N. A., Sunyaev R. A., 2003, Astronomy Letters, 29, 791

Mazzotta P., Rasia E., Moscardini L., Tormen G., 2004, MNRAS, 354, 10

Melrose D. B., 1968, APSS, 2, 171

Monaghan J. J., 1997, Journal of Computational Physics, 136, 298

Monaghan J. J., Gingold R. A., 1983, Journal of Computational Physics, 52, 374

Morris J. P., Monaghan J. J., 1997, Journal of Computational Physics, 136, 41

Norman M. L., Bryan G. L., 1999, LNP Vol. 530: The Radio Galaxy Messier 87, 106

Ohno H., Takizawa M., Shibata S., 2002, ApJ, 577, 658

O'Shea B. W., Nagamine K., Springel V., Hernquist L., Norman M. L., 2003, ApJ in press, astro-ph/0312651

Poludnenko A. Y., Frank A., Blackman E. G., 2002, ApJ, 576, 832

Puchwein E., Bartelmann M., Dolag K., Meneghetti M., 2005, A&A in press, astro-ph/0504206

Ricker P. M., Sarazin C. L., 2001, ApJ, 561, 621

Roettiger K., Loken C., Burns J. O., 1997, ApJS, 109, 307

Sarazin C. L., 1999, ApJ, 520, 529
Schindler S., Mueller E., 1993, ApP, 272, 137
Schlickeiser R., Sievers A., Thiemann H., 1987, ApP, 182, 21
Schuecker P., Böhringer H., Reiprich T. H., Feretti L., 2001, ApP, 378, 408
Schuecker P., Finoguenov A., Miniati F., Böhringer H., Briel U. G., 2004, ApP, 426, 387
Sod G. A., 1978, Journal of Computational Physics, 27, 1
Springel V., 2005, astro-ph/0505010
Springel V., Hernquist L., 2002, MNRAS, 333, 649
Springel V., Yoshida N., White S., 2001, New Astronomy, 6, 79
Steinmetz M., 1996, in IAU Symp. 171: New Light on Galaxy Evolution, 259
Subramanian K., Shukurov A., Haugen N. E. L., 2005, astro-ph/0505144
Sunyaev R. A., Norman M. L., Bryan G. L., 2003, Astronomy Letters, 29, 783
Takizawa M., 2005, ApJ in press, astro-ph/0505274
Tormen G., Bouchet F., White S., 1997, MNRAS, 286, 865
Tormen G., Moscardini L., Yoshida N., 2004, MNRAS, 350, 1397
White S. D. M., Briel U. G., Henry J. P., 1993, MNRAS, 261, L8
Yoshida N., Sheth R., Diaferio A., 2001, MNRAS, 328, 669